TAMPEREEN TEKNILLINEN YLIOPISTO
TAMPERE UNIVERSITY OF TECHNOLOGY

Risto Vehmas

Computational Algorithms for Improved Synthetic Aperture Radar Image Focusing

Julkaisu 1586 • Publication 1586

Tampere 2018

Tampereen teknillinen yliopisto. Julkaisu 1586
Tampere University of Technology. Publication 1586

Risto Vehmas

Computational Algorithms for Improved Synthetic Aperture Radar Image Focusing

Thesis for the degree of Doctor of Philosophy to be presented with due permission for public examination and criticism in Rakennustalo Building, Auditorium RG202, at Tampere University of Technology, on the 26th of October 2018, at 12 noon.

Tampereen teknillinen yliopisto - Tampere University of Technology
Tampere 2018

Doctoral candidate: Risto Vehmas
Laboratory of Signal Processing
Faculty of Computing and Electrical Engineering
Tampere University of Technology
Finland

Supervisor: Prof. Dr. Ari Visa
Laboratory of Signal Processing
Faculty of Computing and Electrical Engineering
Tampere University of Technology
Finland

Pre-examiners: Asst. Prof. Dr. Jaan Praks
Department of Electronics and Nanoengineering
Aalto University
Finland

Dr. Jan Torgrimsson
Department of Earth and Space Sciences
Chalmers University of Technology
Sweden

Opponent: Dr.-Ing. Rolf Scheiber
Microwaves and Radar Institute
German Aerospace Center
Germany

ISBN 978-952-15-4227-5 (printed)
ISBN 978-952-15-4236-7 (PDF)
ISSN 1459-2045

Abstract

High-resolution radar imaging is an area undergoing rapid technological and scientific development. Synthetic Aperture Radar (SAR) and Inverse Synthetic Aperture Radar (ISAR) are imaging radars with an ever-increasing number of applications for both civilian and military users. The advancements in phased array radar and digital computing technologies move the trend of this technology towards higher spatial resolution and more advanced imaging modalities. Signal processing algorithm development plays a key role in making full use of these technological developments.

In SAR and ISAR imaging, the image reconstruction process is based on using the relative motion between the radar and the scene. An important part of the signal processing chain is the estimation and compensation of this relative motion. The increased spatial resolution and number of receive channels cause the approximations used to derive conventional algorithms for image reconstruction and motion compensation to break down. This leads to limited applicability and performance limitations in non-ideal operating conditions.

This thesis presents novel research in the areas of data-driven motion compensation and image reconstruction in non-cooperative ISAR and Multichannel Synthetic Aperture Radar (MSAR) imaging. To overcome the limitations of conventional algorithms, this thesis proposes novel algorithms leading to increased estimation performance and image quality. Because a real-time imaging capability is important in many applications, special emphasis is placed on the computational aspects of the algorithms.

For non-cooperative ISAR imaging, the thesis proposes improvements to the range alignment, time window selection, autofocus, time-frequency-based image reconstruction and cross-range scaling procedures. These algorithms are combined into a computationally efficient non-cooperative ISAR imaging algorithm based on mathematical optimization. The improvements are experimentally validated to reduce the computational burden and significantly increase the image quality under complex target motion dynamics.

Time domain algorithms offer a non-approximated and general way for image reconstruction in both ISAR and MSAR. Previously, their use has been limited by the available computing power. In this thesis, a contrast optimization approach for time domain ISAR imaging is proposed. The algorithm is demonstrated to produce improved imaging performance under the most challenging motion compensation scenarios. The thesis also presents fast time domain algorithms for MSAR. Numerical simulations confirm that the proposed algorithms offer a reasonable compromise between computational speed and image quality metrics.

Preface

The research presented in this thesis was carried out at the Finnish Defence Research Agency (FDRA) and at the Department of Signal Processing, Tampere University of Technology (TUT), during the years 2015 – 2018. Most of the results were obtained during research projects funded by the Finnish Scientific Advisory Board for Defence (MAanpuolustuksen TIeteellinen NEuvottelukunta, MATINE), whose financial support is gratefully acknowledged.

I would like to express my gratitude to my former superiors, Antti Tuohimaa and Jouko Haapamaa at FDRA, and my current superior, Juha Jylhä at TUT, for providing me the opportunity to carry out this research. Special thanks to all of my colleagues both at FDRA and at TUT for putting up with me and for all the help you have provided during the course of this work. I am also very grateful to my pre-examiners Asst. Prof. Jaan Praks from Aalto University and Dr. Jan Torgrimsson from Chalmers University of Technology for providing me valuable feedback concerning the thesis. I also want to thank Dr.-Ing. Rolf Scheiber from the Microwaves and Radar Institute of the German Aerospace Center for serving as my opponent in the public examination of this thesis.

Tampere, September 2018
Risto Vehmas

Contents

Acronyms

ATI	Along-Track Interferometry
BP	Back-Projection
COA	Contrast Optimization Autofocus
CPI	Coherent Processing Interval
CSA	Chirp Scaling Algorithm
DBF	Digital Beam-Forming
DE	Differential Evolution
FFBP	Fast Factorized Back-Projection
FFT	Fast Fourier Transform
FIR	Finite Impulse Response
GPS	Global Positioning System
HRWS	High-Resolution Wide-Swath
ISAR	Inverse Synthetic Aperture Radar
ISLR	Integrated Side-Lobe Ratio
LFM	Linear Frequency Modulation
MSAR	Multichannel Synthetic Aperture Radar
MTI	Moving Target Indication
RCM	Range Cell Migration
RCS	Radar Cross Section
RDA	Range-Doppler Algorithm
RMA	Range Migration Algorithm
RSA	Range Stacking Algorithm
SAR	Synthetic Aperture Radar
SAS	Synthetic Aperture Sonar

SDRS Software Defined Radar Sensor

SNR Signal to Noise Ratio

STAP Space Time Adaptive Processing

STFT Short Time Fourier Transform

TFR Time-Frequency Representation

ULA Uniform Linear Array

PGA Phase Gradient Autofocus

PSLR Peak to Side-Lobe Ratio

PSP Principle of Stationary Phase

PTR Point Target Response

PRF Pulse Repetition Frequency

Nomenclature

The various symbols used throughout the thesis are listed here. The following is not an exhaustive list of all the symbols that are used. Special meaning to different symbols is indicated by the use of subscripts and superscripts. Their significance is explained whenever used, if their meaning is not evident from the context. Boldface letters denote vectors or matrices, whose dimensions are specified when they are defined.

Latin alphabet

a	basis function coefficient
A	amplitude envelope function
B	frequency bandwidth
c	speed of light
D	diameter of an Uniform Linear Array (ULA)
d	element spacing in an ULA
f	basis function
g	reflectivity function
$\widehat{g}$	an estimate of g
G	Fourier transform of g
H	loss function in range alignment
I	intensity image
k	spatial frequency variable
L	loss function in different contexts
M	number of slow-time samples
n	receiver index
N	number of receivers
p	sum envelope of ss
P	S-method window function
r	radial distance (range) variable
$ss(r,t)$	radar signal as a function of range and slow-time
$sss(n,r,t)$	radar signal as a function of receiver number, range, and slow-time
t	slow-time variable
T	slow-time window length
x, y, z	Cartesian spatial coordinates

Greek alphabet

α	angle of arrival
β	azimuth angle
γ	angle coordinate in a local polar coordinate system

δ	Dirac delta symbol
ϵ	step length in gradient descent
ζ	step length in gradient descent
η	range shift
θ	aspect angle
Θ	aspect angle support
λ	carrier wavelength
Π	rectangle function
ρ	range coordinate in a local polar coordinate system
τ	scaled slow-time variable
ϕ	phase function
Φ	Cohen's kernel function
ψ	contrast metric in range alignment
Ψ	contrast metric in autofocus
Ω	S-method window length

Other basic notation

$\mathcal{F}\{\cdot\}$	Fourier transform
$\mathcal{F}^{-1}\{\cdot\}$	inverse Fourier transform
$\mathcal{K}\{\cdot\}$	keystone formatting operation
$\mathcal{R}\{\cdot\}$	rotation operation
$\mathfrak{R}\{z\}$	real part of a complex number z
$\mathfrak{I}\{z\}$	imaginary part of a complex number z
z^*	complex conjugate of z
$f * g$	convolution between f and g
$f \star g$	cross-correlation between f and g
$\angle\{z\}$	phase angle of z

Throughout the thesis, the double letter notation for the SAR signal introduced by Raney in [1] is used. In this notation, the first letter in *ss* corresponds to the range (fast-time) variable and the second to the slow-time variable. Lowercase letters correspond to the spatial or temporal domain and uppercase letters denote the signal in the corresponding frequency domain. Correspondingly, we adopt the notation *sss* for the MSAR signal, where the first letter corresponds to the receiver index.

List of Publications

This is a compilation thesis based on the following original publications which are referred to as I-VI throughout the text. The publications are reproduced with kind permissions from the publishers.

I R. Vehmas, J. Jylhä, M. Väilä, J. Kylmälä, "A Computationally Feasible Optimization Approach to Inverse SAR Translational Motion Compensation", *2015 European Radar Conference (EuRAD)*, Paris, France, pp. 17 – 20, September 2015

II R. Vehmas, J. Jylhä, M. Väilä, A. Visa, "ISAR Imaging of Non-cooperative Objects with Non-uniform Rotational Motion", *2016 IEEE Radar Conference (RadarConf)*, Philadelphia, PA, USA, pp. 1 – 6, May 2016

III R. Vehmas, J. Jylhä, M. Väilä, A. Visa, "Analysis and Comparison of Multichannel SAR Imaging Algorithms", *2017 IEEE Radar Conference (RadarConf)*, Seattle, WA, USA, pp. 340 – 345, May 2017

IV R. Vehmas, J. Jylhä, M. Väilä, J. Vihonen, A. Visa, "Data-Driven Motion Compensation Techniques for Noncooperative ISAR Imaging", *IEEE Transactions on Aerospace and Electronic Systems*, vol. 54, no. 1, pp. 295 – 314, February 2018

V R. Vehmas, J. Jylhä, "Improving the Estimation Accuracy and Computational Efficiency of ISAR Range Alignment", *2017 European Radar Conference (EURAD)*, Nürnberg, Germany, pp. 13 – 16, October 2017

VI R. Vehmas, J. Jylhä, "A Contrast Optimization Algorithm for Back-Projection Image Reconstruction in Noncooperative ISAR Imaging", *EUSAR 2018; 12th European Conference on Synthetic Aperture Radar*, Aachen, Germany, pp. 464-469, June 2018

1 Introduction

As remote sensing and surveillance instruments, radars have several advantages over instruments utilizing shorter wavelengths of the electromagnetic spectrum such as optical, infrared or hyperspectral cameras. The advantages include the capability to measure time delay (which is equivalent to radial distance) very precisely, the fact that radar provides its own illumination, and that it is mostly unaffected by weather conditions such as clouds, smoke or fog [2–4]. The rapid advancement of semi-conductor technology has enabled a variety of radar applications for industrial, consumer, and automotive markets [5]. Due to the advancements in digital computing technology, the functionality of the radar is becoming more and more controlled by computer software and digital signal processing algorithms. The term Software Defined Radar Sensor (SDRS) [6] has been coined to illustrate this tendency.

Synthetic Aperture Radar (SAR) and Inverse Synthetic Aperture Radar (ISAR) are remote sensing instruments operating in the microwave region of the electromagnetic spectrum [7–9]. They are used for high resolution imaging of the ground (SAR) and moving objects (ISAR). The reconstruction of the radar images is based on utilizing the relative motion between the radar sensor and the imaged scene. The radar system can be mounted on an aircraft or a spacecraft (SAR) or it can monitor moving objects while stationary (ISAR). The relative motion is used to synthesize the effect of a very long antenna producing a very narrow antenna beamwidth corresponding to high spatial resolution. SAR is used for such purposes as area (land or sea) monitoring, creating high precision digital elevation models, military reconnaissance, and disaster monitoring, to name a few [10, 11]. ISAR can be used for air- and maritime surveillance and it provides useful information for non-cooperative target recognition [12]. Multichannel Synthetic Aperture Radar (MSAR) is a form of SAR where multiple receive channels are used to receive the signal. It provides increased performance e.g. for Moving Target Indication (MTI) and space-borne SAR imaging. Modern state-of-the-art SAR and ISAR systems can achieve a spatial resolution of about one decimeter [10, 11].

Fig. 1.1 provides an example of a very high resolution radar image. The radar image in this thesis is defined as a two-dimensional representation of the object's radar reflectivity in the spatial domain. The magnitude of the reflectivity is represented by the color scale of the image. In the two-dimensional case, the image is the projection of the object's reflectivity into the ground plane, and thus provides a view of the object as it would be seen from above. To obtain a highly focused image such as the one in Fig. 1.1, the relative motion between the scene and the radar has to be known to within a fraction of the carrier wavelength. In X-band for example, this means a precision of a few millimeters. For airborne SAR, a coarse motion estimate is provided by Global Positioning System (GPS) and inertial measurements units, whereas in non-cooperative ISAR the motion of the object is totally unknown a priori. Data-driven motion compensation is the process

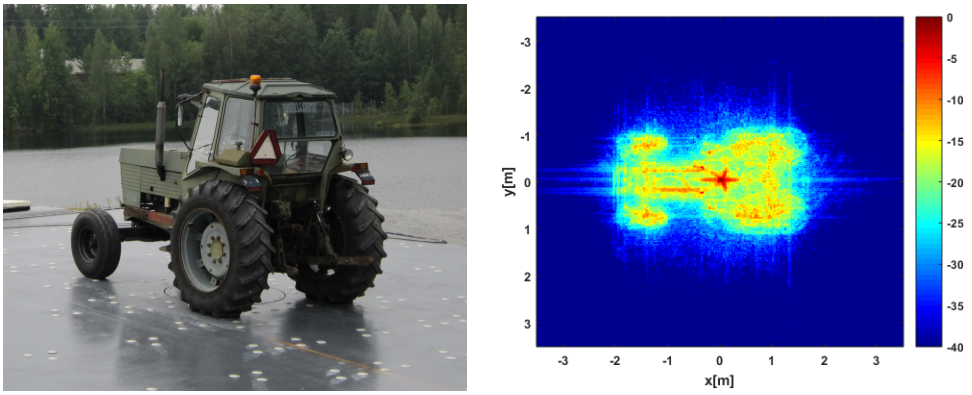

Figure 1.1: The radar image (right) of an object (left) is a two-dimensional representation of the object's radar reflectivity as a function of spatial position. The color scale of the image represents the magnitude of the reflectivity.

of estimating the unknown motion parameters using only information provided by the received signal itself. This process becomes increasingly important as the desired image resolution becomes higher.

1.1 Motivation

Some of the most important current technological trends governing the development of radar systems are illustrated in Fig. 1.2. Modern radar technology enables the use of larger and larger bandwidths for the radar signal producing a higher range resolution. The advancements in phased array and digital computing technologies make it possible to increase the number of separate receive channels, all of which are digitized and stored on receive. The increased number of receive channels allows for great flexibility in the digital signal processing. The increased digital computing power that is available makes it possible to process the radar data in novel ways to provide useful information about the surroundings of the radar.

The three important factors of Fig. 1.2 motivate the development of new signal processing algorithms for various radar applications. In this thesis, the considered application is radar imaging with ISAR and MSAR. For ISAR, the increased spatial resolution necessitates the development of new data-driven motion compensation algorithms. This is due to the inherent approximations in well-established algorithms. The approximations start to break down as the resolution becomes higher causing the conventional methods to be performance limited. The increased number of receive channels provides a large number of opportunities for MSAR algorithm development. Moreover, the increased digital computing power enables the use of more generally applicable algorithms for image reconstruction in both MSAR and ISAR.

The performance of MSAR and ISAR imaging algorithms has historically been limited because of the limited available computation power. For most applications, the signal processing should be carried out in real time. The well-established ISAR and MSAR algorithms achieve this by using suitable simplifications, which for example enable the use of Fast Fourier Transform (FFT)-based correlation techniques. With the increasing computing power, it is possible to overcome these limitations providing increased imaging

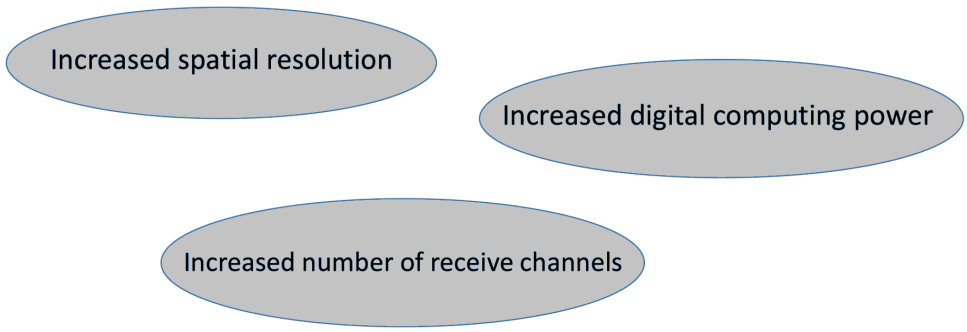

Figure 1.2: The important technological trends driving the development of radar systems. Importantly, these developments enable the radar to obtain more information with better quality about its surrounding environment.

performance. Thus, algorithm development plays a key role in making full use of all the technological developments depicted in Fig. 1.2.

1.2 Background

This thesis focuses on motion compensation and image reconstruction algorithms for ISAR and MSAR. To develop generally applicable algorithms offering the potential for increased imaging performance, it is important to understand the historical perspective and current state-of-the-art of the existing algorithms. Next, an overview of the most prominent existing methods for motion compensation in non-cooperative ISAR and image reconstruction in MSAR imaging is presented.

Data-driven motion compensation algorithms

Since the reconstruction of the radar image requires the knowledge of the relative motion between the radar and the object, non-cooperative ISAR imaging is not possible without some sort of data-driven motion compensation. Motion compensation is normally the first step in the ISAR image reconstruction process. Image quality (e.g. in terms of spatial resolution and image contrast) strongly depends on the accuracy of the motion compensation. Several algorithms for accomplishing motion compensation have been proposed in the literature. In general, data-driven motion compensation in non-cooperative ISAR imaging is a very challenging task. Existing methods are based on suitable approximation and compromises. Many of the state-of-the-art methods rely on several distinct optimization steps, where suitable loss functions are minimized to obtain estimates for the unknown motion parameters [13–17].

Motion compensation in non-cooperative ISAR is usually divided in two distinct parts: translational motion compensation and rotational motion compensation. Translational motion compensation typically consists of two parts also: range alignment and autofocus. Range alignment provides a coarse estimate for the translational motion. It is usually solved by using a suitable optimization procedure based on quality measures calculated from the amplitude envelopes of the range-compressed signal [14, 15, 18, 19]. In these

approaches, a numerical global optimization procedure is used to produce a coarse estimate for the translational motion of the object. For example, a pattern search optimization algorithm was used in [15].

Autofocus refers to the fine translational motion compensation applied after range alignment. It is a well-studied problem in the context of airborne spotlight mode SAR imaging, and a wide variety of different approaches exists. Two widely utilized autofocus approaches are based on Contrast Optimization Autofocus (COA) [13, 17, 20 – 29] and the Phase Gradient Autofocus (PGA) algorithm [30 – 42]. In COA, the loss function is calculated from the image intensities. Examples include the coefficient of variation of the image intensities or amplitudes [13], the sum of the squared intensities [17, 22], and the entropy of the intensity image [14]. The autofocus problem is essentially a local optimization problem [17], and can thus be solved efficiently for example by first order local optimization algorithms [22, 25]. PGA uses an iterative procedure based on estimation theory to estimate the unknown phase error. It is computationally more efficient than COA, and is often referred to as the gold-standard autofocus algorithm [31].

A time window optimization procedure can be used to obtain a suitable Coherent Processing Interval (CPI) that is used in the ISAR processing [43]. In this method, the optimal CPI is the one that maximizes the ISAR image contrast. As a solution to rotational motion compensation, a technique called keystone formatting partially compensates for the Range Cell Migration (RCM) [44 – 47] caused by the rotational motion of the object. Additionally, a Time-Frequency Representation (TFR) is used often in the image reconstruction to mitigate the effects of non-linear phase histories [43, 45, 46, 48 – 60] caused by the object rotation. The former approach was first introduced in [44] in the context of airborne SAR imaging of moving objects. The approach based on TFRs was introduced in [48, 50] in the 1990s and has since matured into a well-established technique. For example, the S-method was demonstrated to surpass the conventional Fourier transform-based range-Doppler approach in [59]. Another way to handle the rotational motion compensation is to isolate strong point-like scatterers from the intensity image and to track their phase progression in the range-compressed signal. This approach is called prominent point processing [8, 61].

An important part of rotational motion compensation is to scale the cross-range dimension of the image into spatial units. This cross-range scaling is a challenging task with no widely accepted general solution [62 – 65]. Existing approaches are based on either estimating high-order phase coefficients from the range-compressed signal [64, 66, 67] or a suitable optimization approach [68, 69]. The optimization approaches rely on dividing the CPI into two or more parts to produce multiple ISAR images. These images are approximated as scaled and rotated versions of each other. Maximizing their correlation can be used to estimate the rotation between them, and the estimated rotation can be used to derive the spatial scale of the image in the cross-range dimension.

An attractive approach to ISAR imaging is to utilize a multistatic system. This refers to a multichannel ISAR system, which can contain multiple transmitters as well as receivers in different spatial positions. The multistatic setup can help in the cross-range scaling problem and in other aspects of the motion compensation as well [70, 71]. The additional information provided by the multiple receiver signals can for example be used to obtain least-squares estimates for the unknown motion parameters of the object [70]. Due to the more complicated imaging geometry, time domain image reconstruction is preferred in the multistatic case [70]. However, the use of time domain image reconstruction algorithms such as [70, 72] in ISAR has been limited, because the data-driven motion compensation

becomes computationally infeasible for a real-time implementation.

Motion compensation in spotlight mode SAR follows very similar principles than in ISAR. However, it is generally not as difficult, because the radar platform usually carriers inertial sensors and a differential GPS. When combined, these sensors can produce an estimate for the flight track to a precision of a few decimeters [11]. Assuming a high-end navigation system, the precision can be even more accurate. However, especially in the case of light-weight platforms such as unmanned aerial vehicles, the motion errors can be large. This calls for estimation techniques very similar to ISAR processing [73, 74]. For space-borne SAR data-driven motion compensation is in general unnecessary, since an almost ideal rectilinear trajectory is possible to achieve. However, atmospheric effects can cause phase errors degrading the image quality of space-borne SAR, and autofocus algorithms can be used compensate them.

Compared to ISAR, the implementation of motion compensation algorithms in SAR is associated with some difficulties. For example, the PGA algorithm [32] only works for spotlight mode imagery and the polar format algorithm [75] in its standard form. This means that it has to be modified for other image reconstruction algorithms [40, 76]. As another example, space-dependent motion compensation [77 – 79] is needed when the scene size is large compared to the standoff distance. Furthermore, the computational cost of the COA techniques becomes a bottleneck for time domain reconstruction algorithms. In part for this reason, computationally efficient autofocus algorithms have been developed for the time domain back-projection image reconstruction algorithm in [80 – 82].

Image reconstruction for MSAR

SAR image reconstruction algorithms can be roughly divided in two classes: fast frequency domain algorithms and exact time-domain algorithms. The Range-Doppler Algorithm (RDA) [83, 84], Chirp Scaling Algorithm (CSA) [1, 77, 78, 85], and Range Migration Algorithm (RMA) [79, 86, 87] belong to the first class, while the second class is based on the back-projection algorithm originating from computer-aided tomography [75, 88]. Frequency domain algorithms are based on utilizing the correlation theorem and the FFT algorithm, which significantly reduces the required number of operations in the SAR image reconstruction. For the frequency domain algorithms to be valid, the trajectory of the radar platform needs to be rectilinear and the radar has to be monostatic. On the other hand, time domain algorithms can be used for an arbitrary imaging geometry.

The use of time domain algorithms has been limited because of their large computational cost. Recently, several fast time domain algorithms have been developed [89 – 92]. An important advantage the time domain algorithms have compared to frequency domain algorithms is the fact that the signal does not have to be uniformly sampled in the along-track dimension. Moreover, the trajectory of the radar does not have to be a straight line or a circle (although it simplifies the processing) [93]. Especially with airborne platforms, deviations from the ideal conditions are always present, which result in complicated processing and degraded image quality for fast frequency domain algorithms [79].

The demand for higher spatial resolution and larger area coverage poses contradictory requirements for conventional monostatic SAR systems. The cause of this contradiction is the fact that in the conventional stripmap imaging mode, high spatial resolution in the along-track direction requires a long synthetic aperture, and the unambiguous sampling of the full aperture thus requires a high Pulse Repetition Frequency (PRF) [7, 8, 94]. The spotlight imaging mode can be used to increase the spatial resolution, but at the cost of

reduced area coverage [8]. When conventional waveforms and identical pulses are used to produce a high resolution in the range direction, the PRF sets a limit for the width of the unambiguous range swath. This causes a trade-off between the scene size and spatial resolution that is governed by the imaging geometry and the radar parameters [95, 96].

Several techniques that are based on configurations consisting of multiple receiver apertures have been proposed to overcome the above-mentioned dilemma [94 – 103]. The original idea dates back to 1975, when Cutrona [104] proposed a multiple beam system for Synthetic Aperture Sonar (SAS) to overcome the trade-off between cross-range resolution and unambiguous swath width. From the signal processing point of view, the situation in SAS closely resembles that of space-borne SAR (due to the vastly smaller propagation speed of the signal in water). For this reason, techniques for combining high spatial resolution and large area coverage using multiple receiver apertures have been proposed in the recent SAS literature [105 – 111].

Most of the previous work concerning High-Resolution Wide-Swath (HRWS) MSAR imaging has been done in the framework of space-borne SAR systems, beamforming in the azimuth (or cross-range) direction, and fast frequency domain algorithms [96, 112 – 115]. More recently, the computationally efficient monostatic time domain back-projection algorithms [89, 90] have been modified for bistatic configurations [91, 92]. In addition to the above-mentioned techniques that use beamforming in azimuth, elevation beamforming can also be advantageous especially for space-borne SAR sensors [100, 103].

1.3 Objectives

As discussed above, standard solutions to data-driven motion compensation in ISAR and image reconstruction in MSAR are becoming performance limited. This is because they rely on several approximations which no longer hold true under operating conditions required for achieving a very high resolution ($\approx$ 10 cm). New algorithmic solutions are proposed in this thesis to overcome these limitations. The main objective is

- to develop computationally efficient algorithms with increased imaging performance for ISAR motion compensation and MSAR image reconstruction.

The increased imaging performance refers to quantitative image quality metrics, such as the image contrast and resolution. The computational efficiency concerns the real-time imaging capability of the algorithms. The increased imaging performance should not entail a significantly increased computational burden. Also, the increased imaging performance entails an increased overall applicability for the algorithms.

The main objective can be divided into two secondary objectives:

- To present a unified optimization framework for non-cooperative ISAR imaging, in which the individual pieces of the motion compensation fit together in a seamless manner; and
- to present computationally feasible time domain image reconstruction algorithms for ISAR and MSAR.

The accuracy-efficiency trade-off of the algorithms is an important consideration of this thesis. The aim is to find acceptable trade-offs between image quality and computational

efficiency. For the latter secondary objective, the problem consists of determining suitable approximations and compromises, which reduce the computational complexity of the time domain back-projection algorithm for the MSAR system. In addition, the challenge lies in formulating a well-posed and computationally tractable optimization problem for time domain ISAR image reconstruction.

1.4 Research methods and restrictions

The motion compensation and image reconstruction algorithms presented in this thesis have been implemented and tested with MATLAB software developed by the author. The algorithms have been tested with both simulated and experimental SAR and ISAR data. For non-cooperative ISAR simulations, data were created utilizing the physical optics Radar Cross Section (RCS) simulation tool presented in [116]. The Signature Management Group of the Finnish Defence Research Agency provided the measured turntable data for this thesis. The data from these measurements are used to validate the developed data-driven motion compensation algorithms for ISAR.

In this thesis, only two-dimensional radar imaging is considered. However, some of the methods developed in the thesis can be generalized to work in a three-dimensional setting also. The most important difficulty in the three-dimensional case comes from the additional rotational degrees of freedom. For the MSAR image reconstruction, only an Uniform Linear Array (ULA) antenna was considered. However, the time domain algorithms developed in this thesis can easily be applied to non-uniform array as well. The restriction was done to provide a meaningful comparison with standard algorithms which are only applicable for an ULA.

1.5 Publications and author's contribution

The contributions of the included original publications I – VI are summarized below. The research contribution of this thesis can be roughly divided into two categories as depicted in Fig. 1.3. Publications I, II, and IV – VI present improvements to the conventional optimization-based ISAR processing. Time domain image reconstruction algorithms are considered for ISAR in I and VI and for MSAR in III.

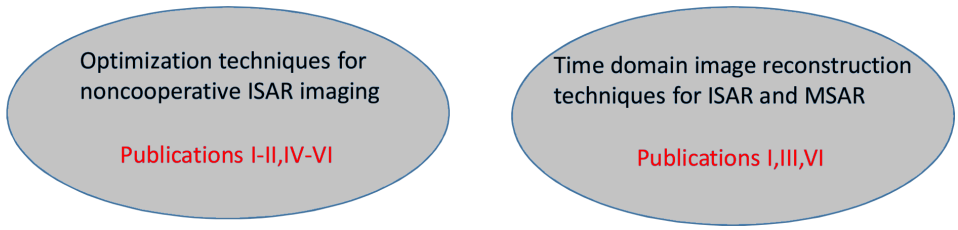

Figure 1.3: The research contribution of the thesis can be divided into two categories as depicted.

I In this paper, we propose an optimization approach to ISAR translational motion compensation based on the global range alignment and COA methods. In range

alignment, we parametrized the track as a spline polynomial and minimized the mean squared envelope difference of the range-compressed signal. Differential Evolution (DE) was used in solving the global numerical optimization problem. The COA problem was solved using first order numerical optimization by deriving an expression for the gradient of the loss function. We considered time domain back-projection image reconstruction but the proposed approach is easily extended to other reconstruction techniques as well.

II The paper proposes optimization techniques for enhancing the ISAR image reconstruction process. Specifically, we utilized keystone formatting and time-frequency signal analysis in an optimization framework for the ISAR image reconstruction. The proposed optimization method estimates the optimal slow-time window by minimizing a loss function depending on the contrast of the sum envelope of the range compressed signal. The optimal kernel function for the Cohen's class TFR was determined by maximizing the contrast of the intensity normalized ISAR image. Furthermore, the time-frequency reassignment method was utilized to enhance the contrast of the ISAR image. In the numerical results, the proposed optimization steps were shown to increase the image contrast.

III The paper formulates the SAR image reconstruction for a multichannel system in its most general form. We utilized Digital Beam-Forming (DBF) and the phase center approximation to develop a fast time domain (Fast Factorized Back-Projection (FFBP)) algorithm for MSAR. We presented two FFBP implementations for MSAR and performed a comparative study between MSAR imaging algorithms. Considering the numerical simulation results, the proposed reconstruction algorithms were significantly faster than exact time domain image reconstruction with essentially the same achieved image quality metrics. The proposed time domain MSAR algorithms provide an alternative for conventional frequency domain image reconstruction, especially in cases where the operating conditions are not ideal for the frequency domain algorithms.

IV The paper describes how optimization can be used in every part of data-driven motion compensation and ISAR image reconstruction. Several improvements were proposed to the range alignment, time-window selection, autofocus, time-frequency-based image reconstruction and cross-range scaling procedures. The range alignment method was enhanced by combining previously suggested loss functions and utilizing first order numerical optimization. In the time window optimization process, we proposed performing autofocus and keystone formatting before evaluating the contrast of the ISAR image. In COA, we utilized a computationally efficient optimization procedure by deriving an expression for the second order partial derivatives of the loss function. For the time-frequency based imaging approach, we chose the optimal kernel for the TFR based on the image contrast. Finally, the rotation correlation and polar mapping methods were combined to solve the cross-range scaling problem in a straightforward manner. By combining all the proposed improvements, a computationally efficient ISAR algorithm was demonstrated. It improved the imaging performance in terms of the image contrast by 50 percent at best and 28 percent on average under complicated target motion dynamics.

V The paper presents methods for improving both the estimation performance and computational efficiency of ISAR range alignment algorithms using mathematical optimization. We proposed new loss functions and a new optimization method

based on the first and second order partial derivatives of the loss function. The new loss functions were introduced to obtain better performance under significant target rotation and very high range resolution. In numerical experiments with very high resolution X-band ISAR data the proposed loss functions were shown to increase the estimation performance as much as 35 percent. Moreover, the proposed numerical optimization method reduced the computational cost of optimization-based range alignment by an order of magnitude.

VI The paper considers ISAR imaging of non-cooperative objects exhibiting challenging unknown motions using the time domain back-projection algorithm. We proposed a contrast optimization approach for the data-driven motion compensation problem, in which a novel approach using the gradient of the loss function was utilized in the optimization. The translation and the rotation of the object were estimated simultaneously using first order numerical optimization. The algorithm utilized the methods of IV to produce initial guesses for the unknown motion parameters to speed up its convergence. In numerical experiments, the proposed optimization approach was able to estimate highly non-linear translational and rotational motions producing well-focused ISAR images.

In all of the included publications, the author has been responsible for deriving the theoretical results, developing and implementing the computational algorithms, performing the numerical experiments, analyzing the results, and writing the manuscripts. The co-authors provided help in designing the numerical experiments, interpreting the results, and provided valuable feedback and suggestions to help improve the manuscripts. The experimental data used in the studies has been provided by the Signature Management Group of the Finnish Defence Research Agency. The comments and suggestions made by the anonymous peer-reviewers also helped improve the quality of the manuscripts.

1.6 Outline

This thesis is divided into 5 chapters. In Chapter 1, the background and motivation for the study are given. They are followed by the objectives, research methods, restrictions and contributions of the thesis. Chapter 2 introduces the basic principles of ISAR and MSAR image reconstruction and motion compensation algorithms. The research contribution of the thesis is summarized in Chapters 3 and 4. Chapter 3 presents the novel algorithms developed for optimization-based data-driven motion compensation in non-cooperative ISAR imaging. Chapter 4 presents the results related to the developed time domain image reconstruction algorithms for both ISAR and MSAR. The achieved results are discussed and critically evaluated in Chapters 3 and 4. Chapter 5 summarizes the most important findings and concludes the thesis.

2 Principles of synthetic aperture imaging and motion compensation

To motivate and understand the algorithms proposed in this thesis, it is essential to have a suitable model for the radar signals of interest. Furthermore, the signal models and their underlying assumptions clarify the significance of different parts of the proposed ISAR and MSAR algorithms. Section 2.1 describes the basic ISAR signal model used for two-dimensional imaging. The concepts of translational and rotational motion compensation are defined and illustrated in Sections 2.2 and 2.3, respectively. Conventional methods for solving them are described. The principles of time domain ISAR image reconstruction are presented in Section 2.4. Section 2.5 concludes the theoretical foundation by introducing the MSAR signal model and the conventional image reconstruction process.

2.1 Basic ISAR principles

Fig. 2.1 illustrates the basic ISAR geometry. The basic ISAR signal model is extensively discussed e.g. in [14, 18, 43, 50, 55, 60, 64, 67, 68]. The model is appropriate for a two-dimensional imaging geometry where the non-cooperative object is constrained to move on a plane. The primed coordinate system, whose origin is assumed to be located in the object's center of mass, is rigidly attached to the object. The spatial degrees of freedom for each instant of slow-time include $\boldsymbol{r}_0$ (the location of object center of mass) and the orientation of the primed coordinate system (the heading of the object). Slow-time t is the time variable that remains constant during the formation of a single range profile and increases from one range profile to the next. Importantly, the aspect angle θ changes as the object moves in a suitable way. Consequently, the range $R_p(t) = ||\boldsymbol{R}_p(t)||$ between every spatial position on the object and the radar changes in a unique way as a function of slow-time.

In most practical ISAR scenarios, we are interested in imaging vehicles such as cars, ships, or airplanes. The distance between the radar and the object is usually several kilometers, whereas the dimensions of the imaged objects are much smaller. Thus, we have $\|\boldsymbol{r}_0\| = r_0 \gg \|\boldsymbol{r}_p\| = r_p$, which means that the object is in the far-field. In IV, we showed how this argument can be used to derive an expression for the distance R_p between an arbitrary point on the object and the radar. The result is

$$R_p(t) \approx r_0(t) + x_p \cos\theta(t) + y_p \sin\theta(t), \tag{2.1}$$

where $x_p = r_p \sin\theta_p$ and $y_p = r_p \cos\theta_p$. This is a key result from the motion compensation perspective, because the motion can be divided into two parts. The first part (r_0) is called the translational motion. It is the same for every image position (spatially invariant) and

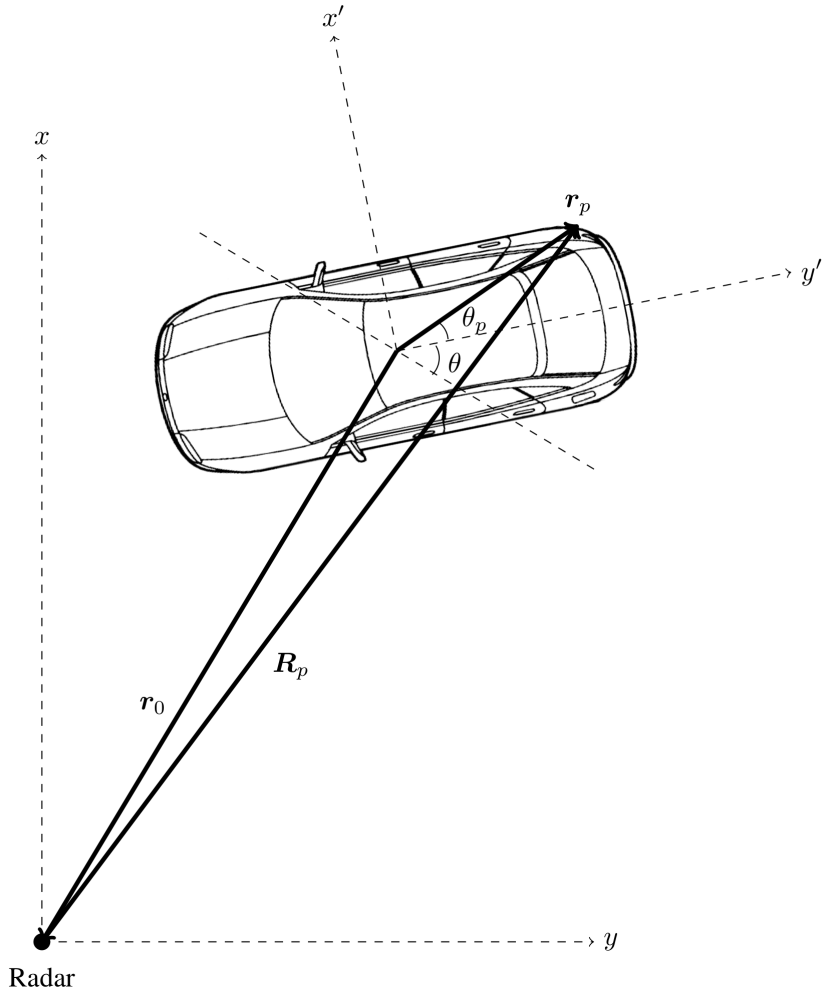

Figure 2.1: Basic ISAR geometry for a vehicle moving on the ground. As the object moves, the distance R_p between an arbitrary point on the object and the radar changes uniquely.

thus is not useful for the image reconstruction. The second part is the rotational motion, which produces the unique phase histories for different image positions (spatially variant) required for obtaining the cross-range resolution.

Adopting the usual start-stop approximation, assuming a constant wave propagation speed, and using the principle of superposition, the Point Target Response (PTR) of the system as a function of radial distance r and slow-time t after range compression and quadrature demodulation is

$$ss_p(r,t) = \operatorname{sinc}\left[\frac{2B}{c}\left(r - R_p(t)\right)\right] e^{-i\frac{4\pi}{\lambda_c}R_p(t)}, \tag{2.2}$$

where λ_c is the carrier wavelength, B is the temporal frequency bandwidth of the signal, and c is the propagation speed of the radio wave. The result (2.2) can be derived by

assuming that the transmitted signal is band-limited [117]. The Fourier transform of (2.2) with respect to the radial distance (range) variable r is

$$Ss_p(k_r, t) = \Pi\left(\frac{k_r c}{2\pi B}\right) e^{-i2(k_r+k_c)[r_0(t)+x_p\cos\theta(t)+y_p\sin\theta(t)]}, \tag{2.3}$$

where k_r is the range spatial frequency variable, $k_c = (2\pi)/\lambda_c$ and Π is the rectangle function. By denoting the reflectivity function of the object as g, we can express the output at the radar receiver as a convolution between the PTR and g. By using the convolution theorem, this yields the result

$$Ss(k_r, t) = e^{-i2(k_r+k_c)r_0(t)}\Pi\left(\frac{k_r c}{2\pi B}\right) G(2k_r\cos\theta(t), 2k_r\sin\theta(t)) \tag{2.4}$$

in the spatial frequency domain. In (2.4), $G(k_x, k_y) = \mathcal{F}_{x\to k_x}\left\{\mathcal{F}_{y\to k_y}\left\{g(x,y)\right\}\right\}$ is the two-dimensional Fourier transform of the reflectivity function g.

The expression in (2.4) is a key result for both ISAR and spotlight mode SAR. It can be interpreted as follows: The range-compressed radar signal is a series of phase-modulated slices of the two-dimensional Fourier transform of the reflectivity function g. The rectangle function in (2.4) represents the fact that the signal is essentially band-limited in k_r. Naturally, the signal also has a limited support in slow-time (and thus in θ), which is omitted in (2.4) for simplicity. Consequently, the slices actually span an annular sector in the two-dimensional spatial frequency domain. In the context of spotlight-mode SAR, the result (2.4) was originally derived by using the projection slice theorem [75, 118].

In non-cooperative ISAR, the difficulty arises from the fact that both r_0 and θ are unknown a priori. To reconstruct a properly focused image, their values as a function of slow-time have to be estimated somehow. As is evident from (2.4), r_0 is a nuisance that does not provide any useful information for the image reconstruction. Its estimation and compensation is referred to as translational motion compensation. Correspondingly, the estimation and compensation of θ is referred to as rotational motion compensation.

2.2 Translational motion compensation

The purpose of translational motion compensation is to estimate r_0 and to compensate for it prior to the ISAR image reconstruction. As indicated by (2.4), the compensation can be achieved in the range spatial frequency-slow-time (k_r, t) domain by multiplying the signal with the complex conjugate of the exponential term on the right hand side of the equation. The space-invariance of the translational motion makes its estimation and compensation more simple than the space-variant rotational motion compensation. The space-invariance can be exploited in the motion compensation algorithms. For example, estimates from several range bins can be averaged in the estimation process to achieve improved estimation performance and the compensation can be achieved by a very computationally efficient complex multiplication in the (k_r, t) domain.

Range alignment

Traditionally, translational motion compensation is performed in two distinct parts: range alignment and autofocus. The purpose of range alignment is to compensate for translational motions larger in magnitude than the range resolution. The estimation process is usually based on quality measures calculated from the shifted amplitude

envelopes of the range-compressed signal [14–16, 19, 119]. According to the Fourier shift property, the linear phase term (as a function of k_r) corresponds to a shift in the range domain. By compensating for the translational phase term in the frequency domain, the range profiles are shifted such that they are "aligned". This is where the term range alignment originates from.

The range alignment algorithms relying on mathematical optimization are based on the minimum entropy method [14] and global range alignment [15, 16]. These methods are optimally suited for small rotational angles and coarse range resolutions, because they approximate that the shape of the amplitude envelope of the range profiles remains constant during the CPI. The basic formulation of these methods is based on minimizing a loss function L, which is a function of the unknown range shifts $\boldsymbol{\eta} \in \mathbb{R}^M$. The value of L quantitatively measures the quality of the range alignment. Thus, the range alignment problem is equivalent to solving

$$\boldsymbol{\eta}^\star = \arg\min L(\boldsymbol{\eta}). \tag{2.5}$$

The global range alignment method is based on quality measures calculated from the sum envelope, which is defined as

$$p(r;\boldsymbol{\eta}) = \sum_{m=0}^{M-1} |ss(r+\eta_m, t_m)|, \tag{2.6}$$

where η_m is the mth component of $\boldsymbol{\eta}$. Using the Fourier shift property, the range-shifted range-compressed signal can be obtained as

$$ss(r+\eta_m, t_m) = \mathcal{F}^{-1}_{k_r \to r}\left\{ e^{i2k_r\eta_m} Ss(r, t_m) \right\}. \tag{2.7}$$

The loss functions of the global range alignment can be expressed as

$$L(\boldsymbol{\eta}) = \int_{-\infty}^{\infty} \psi(p(r,\boldsymbol{\eta}))dr, \tag{2.8}$$

where $\psi : \mathbb{R} \to \mathbb{R}$ is a suitable function used to quantify the quality of the sum envelope. For example, $\psi(p) = -p^2$ is used to measure the contrast and $\psi(p) = -p\log p$ the entropy of the sum envelope. Another loss function used in the literature is the mean squared envelope difference [119], which can be expressed as

$$L(\boldsymbol{\eta}) = \int_{-\infty}^{\infty} \sum_{m=0}^{M-2} \left(|ss(r+\eta_{m+1}, t_{m+1})| - |ss(r+\eta_m, t_m)| \right)^2 dr. \tag{2.9}$$

The advantage of (2.9) compared to (2.8) is that scatterer RCM does not degrade its performance as significantly, because only adjacent time samples (range profiles) are subtracted in the loss function. As a downside, this may cause error accumulation.

As we have shown in V, the loss functions of the type (2.8) are not convex. Consequently, solving the range alignment requires global numerical optimization, which is computationally very demanding. Moreover, heuristic numerical global optimization methods do not guarantee that the optimal solution is even found. The minimum entropy method [14] circumvents this difficulty by using only two adjacent slow-time samples (range profiles) in the definition of the sum envelope (2.6). The method proceeds to solve these $M-2$

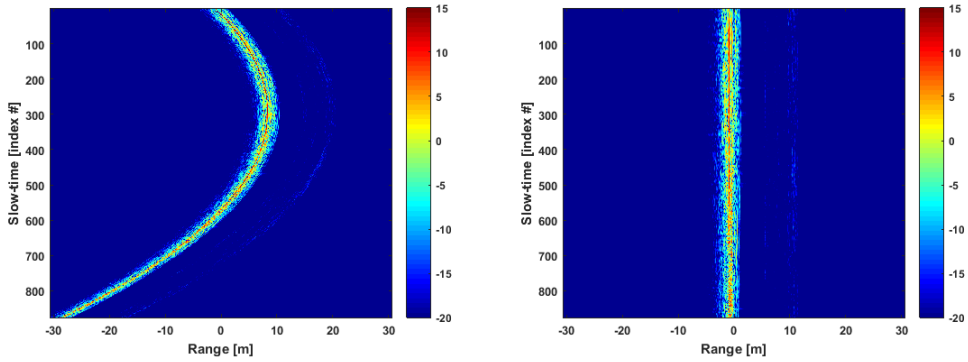

Figure 2.2: The intensity of the range-compressed signal before (left) and after (right) range alignment. The translational motion of the object shifts the response in range and the range alignment compensates for this slow-time-dependent shift.

one-dimensional optimization problems separately. Rapid changes in the target reflectivity as well as the possibility of error accumulation cause problems for this approach. Global range alignment [15, 16] avoids error accumulation and is more robust against target scintillation. However, it comes with the cost of numerical global optimization in a multi-dimensional search space. In [15], a pattern search algorithm and a polynomial model for the range shifts were used to produce a computationally realizable algorithm.

Fig. 2.2 illustrates the effects of translational motion and the result of range alignment in ISAR processing. The signal in question is measured radar data of the object depicted in Fig. 1.1. As indicated by (2.4), the translation of the object manifests itself as a slow-time dependent range shift of the object's radar response. The range alignment eliminates these shifts and aligns the range profiles as a function of slow-time.

Autofocus

After range alignment is performed, a slow-time-dependent phase error caused by the residual translational motion remains in the signal. In conventional ISAR processing, it is assumed that the range alignment has compensated for the translational motions that are larger in magnitude than the range resolution. Thus, taking the inverse Fourier transform of (2.4) after applying the range alignment phase correction results in

$$ss(r,t) \approx e^{i\phi_e(t)} \iint_{-\infty}^{\infty} g(x_p, y_p) ss_p(r,t) dx_p dy_p, \tag{2.10}$$

where ϕ_e is the residual phase error. If this holds true, the residual translational motion can be compensated for by applying a one-dimensional phase correction in the range-slow-time (r,t) domain. The estimation and compensation of this spatially invariant phase term is a widely studied problem in spotlight mode SAR [8, 17, 22, 25, 35, 42, 118, 120, 121]. This computer-automated image focusing procedure is called autofocus. The most prominent autofocus algorithms are based either on the PGA algorithm [30, 32] or COA (also known as sharpness maximization and entropy minimization in the literature) [13, 14, 17, 22, 25].

To arrive at the PGA and COA algorithms, it is useful to consider the simplest algorithm for image reconstruction in non-cooperative ISAR. Using the far-field and small angle

approximations, we can approximate the PTR as

$$ss_p(x,\theta) = \operatorname{sinc}\left[\frac{2B}{c}(x - x_p)\right] e^{-i2k_c(x_p + y_p\theta)}. \tag{2.11}$$

In (2.11), t has been replaced by the aspect angle θ (without any loss of generality, because the PTR depends on t only through θ) and the radial distance variable r is approximated by the Cartesian coordinate x. This approximation is accurate when the object dimension is very small compared to the standoff distance r_0. Substituting (2.11) into (2.10) results in

$$ss(x,\theta) = e^{i\phi(\theta)} e^{-i2k_c x} \mathcal{F}_{2k_c y \to \theta}\left\{ g(x,y) *_x \operatorname{sinc}\left[\frac{2B}{c}(x - x_p)\right]\right\}, \tag{2.12}$$

where the notation $*_x$ stands for convolution with respect to x. Thus, to reconstruct the image (an estimate of g), an inverse Fourier transform with respect to θ suffices provided that the phase error ϕ_e is compensated for prior to it. This simple approach based on a one-dimensional inverse Fourier transform is called the range-Doppler algorithm in the ISAR literature [122]. There also exists an algorithm called range-Doppler for stripmap mode SAR image reconstruction [83], which is not to be confused with this ISAR algorithm.

To produce a focused ISAR image of the object, the phase error ϕ_e in (2.12) needs to be compensated for prior to the image reconstruction. PGA estimates ϕ_e by isolating the phase histories of the strongest scatterers in each range bin [30, 32, 118]. The isolation is achieved by a windowing operation in the spatial (x, y) domain, after which the data is Fourier-transformed back to the (x, θ) domain. The algorithm obtains an estimate $\widehat{\phi}_e$ for the phase error based on evaluating

$$\widehat{\phi}_e(\theta) = \int_{-\infty}^{\theta} \angle\left\{ \int_{-\infty}^{\infty} \exp\left(i\angle\left\{ \frac{\partial ss(x,\theta')}{\partial \theta'}\right\}\right) dx\right\} d\theta'. \tag{2.13}$$

In practice, the derivative of the range-compressed signal in (2.13) can be estimated by a simple complex conjugate multiplication procedure followed by the integration over range bins. Because the isolation of strong point-like targets is not perfect and depends on the initial image focus, the PGA algorithm is usually applied iteratively. In spotlight mode SAR imaging, it has been shown to exhibit excellent performance in estimating high-frequency phase errors over a wide variety of scene types [8, 32].

Another widely utilized approach to autofocus in both SAR and ISAR is COA. As its name suggests, it estimates the phase errors by maximizing the image contrast. The method is conceptually very simple and can be expressed as a single simple equation

$$\boldsymbol{\phi}^\star = \underset{\boldsymbol{\phi}\in[-\pi,\pi]^M}{\arg\min}\ L(\boldsymbol{\phi}), \tag{2.14}$$

where $\boldsymbol{\phi}_m = \widehat{\phi}_e(t_m)$. The loss function L is calculated from the image intensities as

$$L(\boldsymbol{\phi}) = \iint_{-\infty}^{\infty} \Psi(I(\boldsymbol{\phi}; x, y))\, dx\, dy, \tag{2.15}$$

where $I(\boldsymbol{\phi}; x, y) = |sS(\boldsymbol{\phi}; x, y)|^2$ is the image intensity and

$$sS(\boldsymbol{\phi}; x, y) = \mathcal{F}^{-1}_{\theta_m \to y}\left\{ ss(x, \theta_m) e^{-i\phi_m}\right\}. \tag{2.16}$$

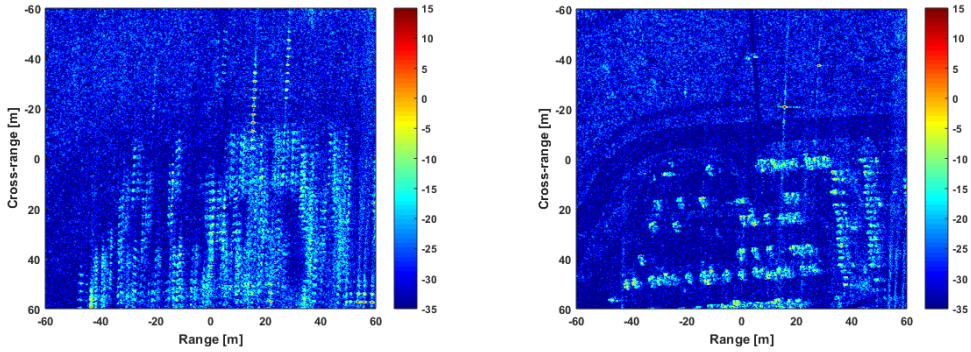

(a) SAR image before autofocus.

(b) SAR image after autofocus.

Figure 2.3: Illustration of the effects of uncompensated motion errors and autofocus in SAR images. Phase errors cause the image to be out of focus in (a), while autofocus sharpens the image in (b) by correcting the phase errors in the data.

The function Ψ is sometimes called the contrast metric [17]. Common choices for it include the power law $\Psi(I) = -I^a$, where $a \in \mathbb{R}$ and usually $a > 1$, and the entropy $\Psi(I) = -I \ln I$. The earliest COA methods were based on using a parametric model for the phase errors and applying black-box numerical optimization techniques [13, 14]. The drawback of these methods was the high computational burden caused by the optimization algorithm. Fienup introduced a computationally efficient first order optimization procedure for COA in [23, 25] by deriving expressions for the gradient under the conventional spotlight SAR paradigm. Since then, COA has matured in a well-established approach in both SAR and ISAR autofocus. COA works generally well for objects and scenes containing bright point-like targets.

Fig. 2.3 illustrates the image defocusing caused by phase errors and the subsequent image focusing using an autofocus algorithm. The spotlight SAR data-set used for this demonstration is from the Gotcha challenge project [123]. The scene consists of a parking lot and the road surrounding it. The resolution of the image is approximately one foot in both directions. The uncompensated phase errors in the data cause the SAR image to be severely defocused, as seen form Fig. 2.3a. The responses of the scatterers are smeared in the cross-range direction of the image, which causes a loss of resolution and image contrast. The defocusing effect is the same throughout the image (spatially invariant). Applying the PGA algorithm to the image data in Fig. 2.3a produces the well-focused SAR image in Fig. 2.3b as a result.

2.3 Rotational motion compensation

Let us consider the signal model (2.4) assuming that the phase term caused by the translational motion of the object has been completely compensated for. To obtain an estimate for the object reflectivity function, the aspect angle θ has to be known. The purpose of rotational motion compensation is to estimate θ and to compensate for its effects in the image reconstruction. In general, rotational motion compensation is a more difficult task than translational motion compensation. The reason for this is the fact that it causes spatially variant effects in the image.

Keystone formatting

To consider the need for rotational motion compensation, it is illustrative to express the signal model as

$$ss(r,\theta) = \iint_{-\infty}^{\infty} g(x,y)\mathrm{sinc}\left[\frac{2B}{c}\left(r - x\cos\theta - y\sin\theta\right)\right] e^{-i2k_c(x\cos\theta + y\sin\theta)}dxdy. \quad (2.17)$$

Two important observations can be made from (2.17). Firstly, the amplitude envelope of each scatterer follows the curve $R = x\cos\theta + y\sin\theta$ causing spatially variant RCM. Secondly, the phase term inside the integral is not linear in θ. Essentially, this means that the simple range-Doppler approach based on (2.12) is not adequate to produce a focused image. In the ISAR literature, the first problem has been partially solved by utilizing an approach called keystone formatting [44–46]. The second problem can be handled by replacing the Fourier transform with a suitable TFR [48–50, 52, 54, 55].

The keystone formatting operation is derived by considering the phase of the signal in the (k_r, t) domain. Using (2.3), this can be expressed as

$$\phi_p(k_r,\theta) = 2\left(k_r + k_c\right)R_p(\theta), \quad (2.18)$$

where $R_p(\theta) = x_p\cos\theta + y_p\sin\theta$ (after translational motion compensation). This divides into the carrier term $k_cR_p(\theta)$ and the term $k_rR_p(\theta)$, which determines the range location of the scatterer in the range-compressed signal. RCM occurs if $2R_p$ changes more than the range resolution during the CPI. Substituting the Maclaurin series expansion of R_p into (2.18) results in

$$\phi_p(k_r,t) = 2(k_r + k_c)(R_p(0) + \dot{R}_p(0)\theta + \frac{\ddot{R}_p(0)}{2!}\theta^2 + \mathcal{O}(\theta^3)), \quad (2.19)$$

where $\dot{R} = dR/d\theta$. Examining (2.19) reveals that the RCM caused by any single term in the Taylor expansion can be removed by a suitable change of variables. Most commonly, the linear RCM is removed by making the change of variables $\theta \to \tau$ according to

$$\theta = \left(\frac{k_c\tau}{k_r + k_c}\right). \quad (2.20)$$

In practice, the change of variables in (2.20) is carried out by using an Finite Impulse Response (FIR) filtering-based resampling of the signal. Notably, this operation removes the RCM regardless of $\dot{R}_p$, which means that it simultaneously compensates for the linear RCM of all scatterers.

Time-frequency-based image reconstruction

To avoid image defocusing caused by the rotational motion, the non-linear phase histories of the echoes scattered from different parts of the object need to be taken into account. An effective way of doing this without having to explicitly estimate the aspect angle θ is to replace the inverse Fourier transform used in the range-Doppler approach by a high-resolution TFR. This is a well-established technique in non-cooperative ISAR and several TFRs have been utilized for this purpose in the literature [49–51, 54–60]. Almost all of these methods are based on using a quadratic TFR. Quadratic in this context means that the TFRs are based on a multiplicative comparison of the signal with itself.

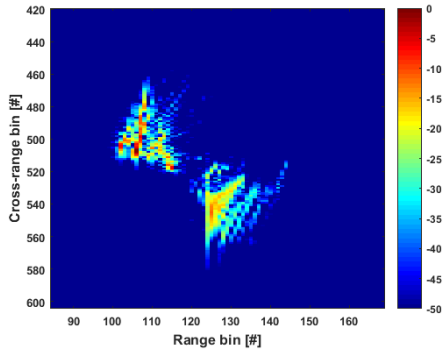

(a) ISAR image before rotational motion compensation.

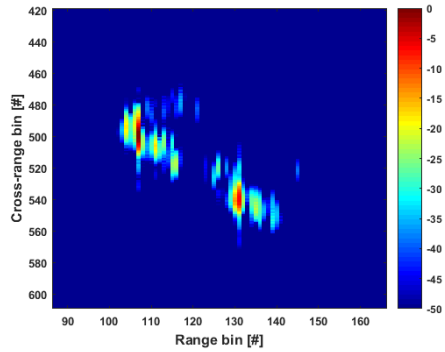

(b) ISAR image after rotational motion compensation.

Figure 2.4: Illustration of the effects of uncompensated rotational motion and rotational motion compensation in ISAR images. Uncompensated non-uniform rotation causes significant spatially variant blurring in (a), which is corrected by the rotational motion compensation algorithm applied in (b).

Quadratic TFRs can be conveniently formulated using the Cohen's class [124]. In this formulation, the TFR and thus the ISAR image reconstruction can be expressed as

$$\widehat{g}(x,y,\theta) = \iint_{-\infty}^{\infty} \Phi(\theta-\mu, y-\nu) WD(x,y,\theta) d\mu d\nu, \tag{2.21}$$

where

$$WD(x,y,\theta) = \mathcal{F}_{\nu\to y}\left\{ ss(x,\theta+\frac{\nu}{2}) ss^*(x,\theta-\frac{\nu}{2})\right\} \tag{2.22}$$

is the Wigner-Ville representation of the signal and Φ is the smoothing kernel function defining the particular distribution. As is evident from (2.21), this method produces a time series of ISAR images of the object. Either the entire time series or a selected subset of images can be exploited in the subsequent image exploitation steps. Although effective in ISAR, the choice of the kernel function is critical for the image reconstruction to be successful. Existing literature provides examples of specific choices but lacks the tools for automatic and optimal choices for the kernel function.

Fig. 2.4 illustrates the effects of uncompensated rotational motion and the benefits of successfully applying rotational motion compensation. The dataset used in this example are is a simulated response of a car in S-band. In this example, the range resolution is very high ($\approx$ 10 cm) and the car rotates almost 30 degrees during the CPI. This causes significant RCM and non-linearity in the phase history of the signal. Without proper compensation, the rotational motion causes significant spatially variant defocusing, as seen in Fig. 2.4a. This defocusing not only decreases the resolution and image contrast, but makes it very hard to determine the shape of the object. After applying keystone formatting and using the S-method as the TFR in (2.21), the ISAR image in Fig. 2.4b is obtained. This time-snapshot is the one where the image contrast is the highest of all the time frames. The spatially variant defocusing is removed and the shape of the object is clearly distinguishable from Fig. 2.4b.

Cross-range scaling

When the ISAR image is reconstructed using a TFR, the rotational motion of the object is not explicitly estimated. In practical terms, this means that the spatial scale of the reconstructed image in the cross-range direction remains unknown. Especially for target recognition applications, it is very important to obtain the correct size of the object in the ISAR image. In the ISAR literature solving the problem of the unknown spatial cross-range scale of the image is referred to as cross-range scaling [64, 66 – 69]. To understand the problem of cross-range scaling thoroughly the relationship between the aspect angle θ and the cross-range extent Y of the reconstructed ISAR image needs to be examined.

Assuming that the translational motion of the object is completely compensated for, the signal model (2.4) can be expressed in the form (neglecting the rectangle functions)

$$Ss(k_r, \theta) = G(2k_r \cos\theta, 2k_r \sin\theta). \tag{2.23}$$

Thus, the aspect angle θ can be interpreted as the cross-range spatial frequency variable $k_y = k_r \sin\theta$ when using this model. Using the Fourier uncertainty relation $Y\Delta k_y = 2\pi$, where Δk_y is the sample spacing of k_y, we can deduce the cross-range extent Y of the image provided that we can estimate Δk_y. Assuming that the signal has a narrow fractional bandwidth, we can use $k_y = 2k_c \sin\theta$. Using an additional small angle approximation, we obtain the result

$$\Delta k_y \approx \frac{4\pi}{\lambda}\Delta\theta. \tag{2.24}$$

Using the result (2.24) in the Fourier uncertainty relation leads to

$$Y = \frac{\lambda}{2\Delta\theta}. \tag{2.25}$$

According to (2.25), the cross-range scaling can be achieved by obtaining an estimate for the angular sample spacing $\Delta\theta$. What complicates this problem is the fact that $\Delta\theta$ is not necessarily constant during the CPI.

The rotation correlation [68] and polar mapping [69] methods are based on an optimization approach. They minimize a loss function to determine $\Delta\theta$. The loss function is the correlation between two sub-aperture images formed from two non-overlapping sub-CPIs of the signal. According to (2.23), using two non-overlapping sub-CPIs is equivalent to using a rotated version of the same signal. The correlation is a function of the amount of rotation that is applied to one of the sub-aperture images. By maximizing the correlation, an estimate for the rotation between the sub-aperture images is obtained and the sample spacing $\Delta\theta$ can be deduced using it.

Time window optimization

A way to achieve improved image quality when dealing with large amounts of recorded ISAR data is to use time window optimization [43, 125, 126]. In [126], the optimum CPI for the ISAR image reconstruction is chosen based on the phase information of prominent points on the target. This provides a way to achieve rotational motion compensation at the same time. The method in [43] chooses a suitable CPI from the long time interval by maximizing the image contrast. Mathematically, this method minimizes the negative image contrast loss function

$$L(\theta_c, \Theta) = \iint_{-\infty}^{\infty} \Psi(|\mathcal{F}_{\theta\to y}\{w(\theta - \theta_c, \Theta)ss(x, \theta)\}|^2)dxdy \tag{2.26}$$

to determine the optimal location θ_c and the shape parameter Θ of a particular window function w. The simplest choice is to use a rectangular window Π. Strictly speaking, this method does not perform translational or rotational motion compensation by itself. Nevertheless, this approach can be used to locate a suitable CPI from the data where the previously mentioned motion compensation algorithms can be applied to the time-windowed data producing a good imaging result.

2.4 Time domain ISAR image reconstruction

Let us now consider what the non-approximated way of image reconstruction in non-cooperative ISAR entails. In its most general form, the image reconstruction is performed by correlating the received signal with the spatially variant PTR of the system. In the two-dimensional ISAR case, the PTR is of the form (2.2). If the amplitude envelope of the impulse response in (2.2) is substituted for a δ-function, the two-dimensional matched filter correlation integral reduces to a one-dimensional integral. This results in the so-called back-projection integral

$$\widehat{g}(x_p, y_p) = \int_{-\infty}^{\infty} ss(R_p(t), t) \exp\left[i \frac{4\pi R_p(t)}{\lambda}\right] dt. \tag{2.27}$$

In non-cooperative ISAR, the difficulty lies in the fact that the translation r_0 and rotation θ determining the form of R_p are not known a priori. To produce any meaningful imaging result using (2.27) they need to be estimated somehow.

Back-projection has not been extensively used in the context of non-cooperative ISAR imaging. This is mostly due to the lack of computationally feasible motion compensation algorithms that can be used with it. For example, the COA approach becomes computationally very intensive, because the image needs to be reconstructed every time the loss function is evaluated. Moreover, when the translational motion compensation is carried out in one step, the local optimization approach of COA is not suitable due to the non-convex nature of the loss function. Back-projection image reconstruction was used in [70, 71] for a multistatic ISAR system. The multistatic setup provides additional degrees of freedom that can be used to successfully estimate the motion parameters of the object. The monostatic case is more difficult, because both the translation and rotation of the object should be estimated simultaneously.

2.5 MSAR image reconstruction

In this section, the background of MSAR imaging is presented. The signal model and the approximations associated with it are discussed. Then, the image reconstruction using conventional fast frequency domain algorithms is introduced.

Signal model

In its most basic form, the MSAR system is an ULA on-board a moving platform. The system is depicted in Fig. 2.5. It consists of a single transmitter antenna (TX) and a linear array of N receivers (RX) spaced distance d apart. For each transmitted waveform, all the receivers digitize and store the received echo signal. This allows for great flexibility in the subsequent digital signal processing. It enables such advanced signal processing techniques as Along-Track Interferometry (ATI) [127], Space Time Adaptive Processing (STAP) [128], and DBF [129] on receive.

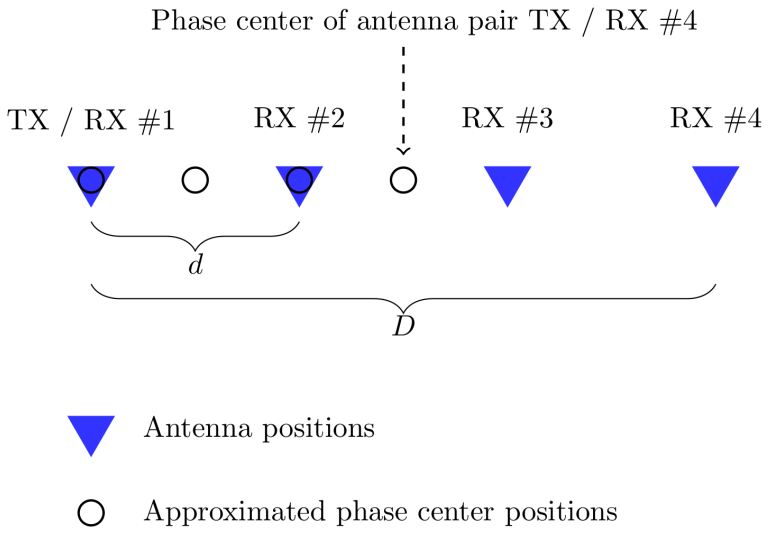

Figure 2.5: Basic geometry of an ULA antenna suitable for an MSAR system. The diagram illustrates the phase center approximation, in which the bistatic geometry is approximated as a monostatic one.

Denoting the position of receiver n as $\boldsymbol{r}_{rx,n} = \boldsymbol{d}_n + \boldsymbol{r}_{tx}$, where $\boldsymbol{d}_n = [0\ nd\ 0]^T$, $n = \lceil -N/2 \rceil, \ldots, \lceil N/2 - 1 \rceil$, and $\boldsymbol{r}_{tx}$ is the position of the transmitter, the position of the transmitter as a function of slow-time $t \in [-T/2, T/2]$ can be expressed as $\boldsymbol{r}_{tx}(t) = \boldsymbol{r}_0 + \boldsymbol{v}t$ with $\boldsymbol{v} = [0\ v\ 0]^T$ and $\boldsymbol{r}_0 = [x_0\ 0\ z_0]^T$, where v is the platform speed. As in the ISAR case, we adopt the start-stop approximation, assume a constant wave velocity, and use the principle of superposition. To obtain a model for the range-compressed signal for a specific waveform, the correlation theorem can be used. For example, for the Linear Frequency Modulation (LFM) waveform the Principle of Stationary Phase (PSP) can be used to express the solution of the correlation integral [84, 129]. Assuming the ground reflectivity function g does not depend on frequency or aspect angle, the model for the MSAR signal can be expressed as the superposition integral

$$sss(n, r, t) = \Pi\left(\frac{t}{T}\right) \iiint_{-\infty}^{\infty} V_{rx,n}(\boldsymbol{r}, t) V_{tx}(\boldsymbol{r}, t) g(\boldsymbol{r}) A(r - \tilde{R}(\boldsymbol{r}; n, t)) e^{-ik_c \tilde{R}(\boldsymbol{r}; n, t)} d\boldsymbol{r}, \tag{2.28}$$

where $\boldsymbol{r} = [x\ y\ z]^T$, $d\boldsymbol{r} = dxdydz$, $A : \mathbb{R} \to \mathbb{R}$ is the amplitude envelope of the range-compressed waveform, $\tilde{R}(\boldsymbol{r}; n, t) = \|\boldsymbol{r}_{tx}(t) - \boldsymbol{r}\| + \|\boldsymbol{r}_{rx,n}(t) - \boldsymbol{r}\|$, $V_{rx,n}$ and V_{tx} are the radiation patterns of the nth receiver and the transmitter, respectively. For the LFM waveform, the amplitude envelope of the range compressed signal can be approximated as $A(r) = \operatorname{sinc}\left(\frac{Br}{c}\right)$. This simplified signal model (2.28) is a starting point for understanding the nature of the SAR image reconstruction process, in which an estimate of g is reconstructed from the received signal sss.

Fig. 2.5 illustrates the MSAR system architecture. The exact geometry of each transmitter-receiver pair is bistatic, but under certain conditions it can be approximated as monostatic. The effective phase center of a single receiver n is located half-way between the transmitter

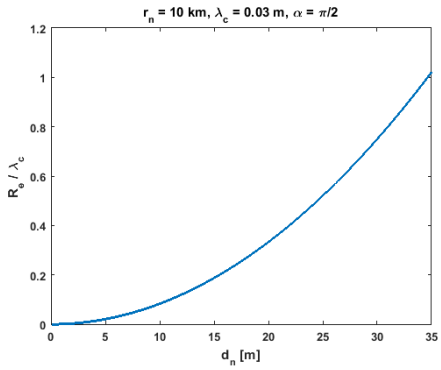

(a) Relative range error for an airborne geometry.

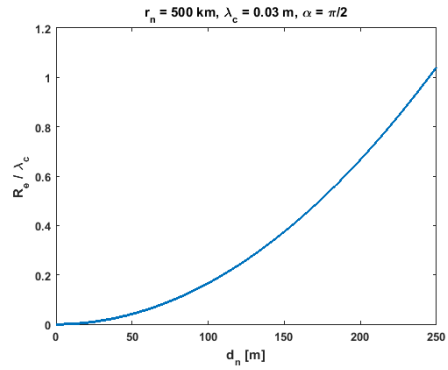

(b) Relative range error for a space-borne geometry.

Figure 2.6: The relative range error of the phase center approximation as a function of the array element spacing d_n for two different geometries. In both cases, the approximation is very accurate for reasonable element spacings within a single platform.

and the receiver n. These effective phase centers can be regarded as approximated monostatic sample positions [95,96,106,107]. This approximation has first been introduced and analyzed in the SAS literature [106,107,130]. The approximation error (the difference between the actual bistatic range and the approximated monostatic range) is

$$R_e = \|\boldsymbol{r}_{tx} - \boldsymbol{r}\| + \|\boldsymbol{r}_{rx,n} - \boldsymbol{r}\| - 2\|\boldsymbol{r}_n\|. \tag{2.29}$$

A second order Maclaurin series expansion yields the result (see e.g. [107] or III)

$$R_e(d_n) \approx \frac{d_n^2}{4r_n}\left(1 + \sin^2\alpha\right) + \frac{d_n^4}{96r_n^3}(11 - 13\sin^2\alpha), \tag{2.30}$$

where $\cos\alpha = \boldsymbol{r}_n^T\boldsymbol{d}_n/||\boldsymbol{r}_n||||\boldsymbol{d}_n||$, and $\boldsymbol{r}_n = (\boldsymbol{r}_{tx} + \boldsymbol{d}_n/2) - \boldsymbol{r}$. The phase center approximation is valid when $R_e \ll \lambda_c$. It is easily verified that the approximation is very accurate when all the receivers are on-board the same air- or space-borne platform. In that case, (2.30) can be further approximated as $d_n^2/(2r_n) \ll \lambda_c$. The approximation error is visualized for both the air- and space-borne geometries in Fig. 2.6. The error has been calculated in the broadside direction ($\alpha = \pi/2$) and assuming an X-band radar system with $\lambda_c = 0.03$ m. In the airborne case seen in Fig. 2.6a, the approximation starts to break down when $d_n > 20$ m. Due to the larger standoff distance r_n in the space-borne case of Fig. 2.6b, the limit is $d_n > 100$ m. The phase center approximation significantly simplifies the subsequent analysis, because multichannel signal (2.28) can be approximated as a monostatic signal when it is valid.

The resolution and sampling requirements follow from the spatial frequency content of the signal. The Fourier uncertainty relation $\Delta y = 2\pi/B_y$ between the sample spacing along the synthetic aperture Δy and the along-track spatial frequency content B_y yields the Nyquist criterion

$$\Delta y < \frac{\lambda_c}{4\sin\left(\frac{\theta_{hp}}{2}\right)}, \tag{2.31}$$

where θ_{hp} is the half-power beamwidth of an individual array element. One of the most important advantages of the MSAR system originates from the along-track sampling

requirements. For a monostatic system, $\Delta y = v/f_{PR}$, where f_{PR} is the PRF. The PRF also determines the size of the unambiguous range swath as $W_r = c/(2f_{PR})$ causing a trade-off between swath width W_r and cross-range resolution δy. Under the phase center approximation, the MSAR system is a monostatic single-channel stripmap system with a half-power beamwidth θ_{hp}. Compared to a real monostatic system, Δy is determined by the element spacing d in addition to f_{PR} (and v). For a real monostatic system to achieve the same sample spacing f_{PR} would have to be N times higher than for the MSAR system. Overcoming the compromise between δy and W_r has been the main motivation for introducing the MSAR techniques in the context of space-borne SAR sensors operating in stripmap mode [94–96, 96–102, 112–115, 129].

Image reconstruction

The exact SAR image reconstruction is done by performing a spatially variant correlation between the received signal (2.28) and the PTR of the SAR system [7, 9, 83, 131]. The PTR of the MSAR system can be obtained by substituting $g(\boldsymbol{r}) = \delta(\boldsymbol{r} - \boldsymbol{r}_p) = \delta(x - x_p)\delta(y - y_p)\delta(z - z_p)$ into the signal model (2.28). This non-approximated way leads to the multichannel back-projection integral

$$\hat{g}(\boldsymbol{r}) = \sum_{n=0}^{N-1} \int_{-\infty}^{\infty} sss(n, \tilde{R}(\boldsymbol{r}; n, t), t) e^{ik_c \tilde{R}(\boldsymbol{r}; n, t)} dt. \tag{2.32}$$

The computational cost of reconstructing the image using (2.32) is proportional to NPM when P is the number of image pixels. For almost any practical application, the computational burden of (2.32) is too high. Even for monostatic high-resolution SAR systems direct back-projection is still seldom used if a real-time imaging capability is needed. Throughout the years, the SAR community has developed a number of computationally efficient image reconstruction algorithms utilizing the special properties of the SAR signal.

The phase center approximation allows for significant computational savings in the MSAR image reconstruction. However, this relies on the assumptions that the synthetic aperture is linear and that the approximated monostatic samples are uniformly spaced. In this simplified case the distance $r_n(\boldsymbol{r}; t) = ||(\boldsymbol{r}_{tx}(t) + \boldsymbol{d}_n/2) - \boldsymbol{r}||$ as a function of slow-time for different y-positions of the scene is simply a shifted version of the function where $y = 0$. In the case of a linear synthetic aperture, we can substitute the slow-time variable t for the along-track coordinate $y_r = vt$ of the radar without loss of generality. In other words, we have

$$r_n([x\ y\ z]^T; y_r) = r_n([x\ 0\ z]^T; y_r - y). \tag{2.33}$$

Under the phase center approximation, the received bistatic samples for each transmitted waveform correspond to monostatic samples in the along-track direction. Thus, the MSAR signal is not a function of three variables but only two, and we can substitute $sss \to ss$. In terms of the PTR the result (2.33) implies that

$$Ss_p([x\ y\ z]^T; k_r, y_r) = Ss_p([x\ 0\ z]^T; k_r, y_r - y). \tag{2.34}$$

Without loss of generality, the Fourier integrals $Ss(k_r, y_n) = \mathcal{F}^{-1}_{k_y \to y_n}\{SS(k_r, k_y)\}$ (and similarly for Ss_p) can be substituted into the matched filter correlation integral. This yields (neglecting unimportant constant factors)

$$\hat{g}(\boldsymbol{r}) = \iint_{-\infty}^{\infty} SS(k_r, k_y) SS_p^*(\boldsymbol{r}; k_r, k_y) dk_r dk_y. \tag{2.35}$$

Using the Fourier shift property and (2.34), (2.35) can be expressed as

$$\begin{aligned}\hat{g}(\boldsymbol{r}) &= \iint_{-\infty}^{\infty} e^{ik_y y} SS(k_r, k_y) SS_p^*([x\ 0\ z]^T; k_r, k_y) dk_r dk_y \\ &= \mathcal{F}_{k_y \to y}^{-1} \left\{ \int_{-\infty}^{\infty} SS(k_r, k_y) SS_p^*([x\ 0\ z]^T; k_r, k_y) dk_r \right\}.\end{aligned} \tag{2.36}$$

The result in (2.36) means that the PTR is needed only once for every x-coordinate, and the inverse Fourier transform in (2.36) produces a single x-slice of the image. The reconstruction via (2.36) is called the Range Stacking Algorithm (RSA) [9, 132]. In other words, since according to (2.34) the shape of the PTR for a fixed x-value is the same for every y-value for a linear synthetic aperture, the correlation in the y-direction can be evaluated using the correlation theorem.

The fact that the image reconstruction (2.36) requires a two-dimensional correlation with a different kernel SS_p for each x-position results in a high computational burden. For this reason, several SAR image reconstruction algorithms have been developed by the SAR community to reconstruct the SAR image in a computationally feasible manner. For a linear synthetic aperture, the reconstruction equation (2.36) can be further simplified by deriving analytic expressions for the Fourier transforms sS_p and SS_p of the PTR. This results in the RDA [7, 83] and RMA (also called the $\omega - k$ and the wavenumber domain algorithm in the literature) [8, 86, 87], respectively. The Fourier transforms cannot be expressed in closed form, but the PSP can be used to produce the required expressions. The CSA [1, 78, 85] compensates the x-dependence of the RCM curves r_n by adjusting the chirp rate of the LFM signal in the (r, k_y) domain prior to range compression. This requires an analytic expression for the uncompressed LFM signal in the (r, k_y) domain, which is again derived by using the PSP [1]. The following processing steps of the CSA rely on additional approximations, which are valid for small fractional bandwidths and small integration angles [8, 85]. The RDA and the RMA require an interpolation to take into account the x-dependence of the PTR, which results from the fact that r_n depends on x (and z). The interpolation in the RMA corresponds to a rescaling of the k_r variable for each k_y value, which removes the x-dependence from the RCM curves r_n. After this operation, a spatially invariant correlation kernel (the same SS_{ptr} for each x) suffices in the SAR image reconstruction. In the RDA a proper rescaling of the range variable r for each k_y corrects the RCM in the (r, k_y)-domain, after which the SAR image reconstruction reduces to a series of one-dimensional correlation integrals.

In order to calculate the Fourier transforms in (2.36) with the FFT algorithm, the signal has to be uniformly sampled in the y_r-direction. As pointed out in [95, 96], this results in stringent requirements for the PRF of the MSAR system if the phase center approximation is to be used. On the other hand, the time domain reconstruction equation (2.32) does not pose such a requirement for the sample spacing. For airborne SAR processing, it is important that the reconstruction algorithm can perform motion compensation accurately. Again, the time domain reconstruction equations work for an arbitrary trajectory, but the frequency domain algorithms are based on the property (2.34), which only holds true for a linear synthetic aperture. This means that the true trajectory has to be corrected to produce a nominal linear trajectory, which is used in the image reconstruction. However, this is not straightforward for all the frequency domain algorithms, since the motion errors cause a change in the travel distance that depends on the scene position $\boldsymbol{r}$. The higher the desired cross-range resolution and the wider the image swath W_r in the range direction, the bigger the resulting error will be if this dependence is not correctly taken into account.

The range stacking reconstruction (2.36) can handle motion errors accurately, since the PTR is explicitly created for each x-position. The RMA and the CSA can also be modified to perform range-dependent motion compensation. These generalizations are called the extended chirp scaling and extended wavenumber domain algorithms [78, 79].

3 Optimization framework for imaging non-cooperative moving objects

Data-driven motion compensation in non-cooperative ISAR imaging is traditionally divided into several distinct and consecutive steps. In every step, suitable approximations are made to develop a computationally realizable algorithm. The motivation behind this approach has been the fact that problem would be too complex and computationally intensive to solve using a more naive and direct approach. As is evident from (2.1)–(2.4), a direct approach would entail estimating the two degrees of freedom (translation and rotation of the object) for every instant of slow-time.

As discussed in Chapter 2, traditional approaches to ISAR processing include range alignment, autofocusing, time-window optimization, cross-range scaling and image reconstruction using a suitable TFR. The approximations used in each of these steps lead to a loss of accuracy in the estimation and motion compensation process. This in turn leads to a loss of imaging performance in terms of image contrast (degree of focus) and spatial resolution. With very high-resolution (≈ 10 cm) ISAR imaging of non-cooperative objects exhibiting complicated motions, the traditional approaches (e.g. [13, 15, 17, 19, 68, 69]) are becoming performance limited.

To achieve increased imaging performance, we have proposed several improvements to the conventional optimization-based ISAR techniques in I–II, and IV–V. Section 3.1 briefly describes the data and methodology used to test the developed algorithms. Sections 3.2–3.6 summarize the proposed improvements for each motion compensation step and present experimental results related to them. The choices made in the algorithms are justified and their critical aspects are highlighted. Section 3.7 concludes this Chapter by discussing the obtained results for the optimization-based ISAR processing.

3.1 Data

Both experimental and simulated ISAR data were used to evaluate the performance of the motion compensation algorithms developed in this thesis. The simulated data used in I and II were created by using a physical optics RCS simulation tool [116]. The experiments in IV–VI were based on measured X-band radar data. The data were obtained using a turntable and a radar system with a stepped-frequency waveform. The measurements were conducted at an open space measurement range while the target vehicles were in the far-field. The radar operated at X-band, and a frequency bandwidth of 1–1.5 GHz was chosen from the data to produce a range resolution of 10–15 cm. During the

(a) Ford Focus. (b) Toyota Corolla. (c) VW Transporter. (d) Valmet. (e) VW Golf.

Figure 3.1: The measured objects of the ISAR experiments considered in IV – VI. The figure is reproduced from IV.

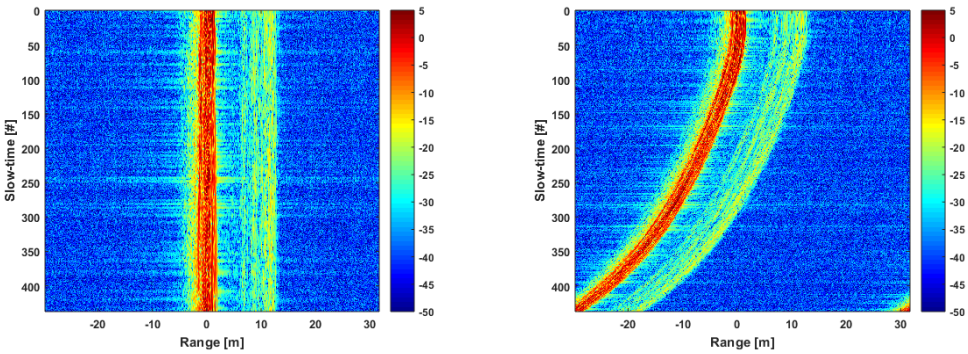

(a) Signal intensity before motion emulation. **(b)** Signal intensity after motion emulation.

Figure 3.2: The intensity of the range-compressed data before (a) and after (b) the motion emulation process. Translational motion is emulated by shifting the signal in range. Non-uniform rotation is obtained by rescaling the slow-time variable.

measurements, the objects rotated through the full 360 degree range of aspect angles. Only a portion of this data was used in the conducted numerical experiments, e.g. in IV a 60 degree aspect interval was chosen.

In IV – VI, the following methodology was used to produce the non-cooperative motion compensation scenarios. Translational motions were emulated by shifting the signal in range utilizing the Fourier shift property in (2.7). To produce a non-uniform rotation for the object, the data were resampled in the slow-time dimension using an FIR interpolator. Both the translation and rotation were chosen to be polynomial functions of slow-time with a varying degree and randomly chosen coefficients. This way, it was possible to test a large number of challenging motion compensation scenarios for benchmarking the algorithms. Since the ground truth of the motions was available, it was easy to evaluate the estimation performance of the algorithms. The detailed descriptions of the used data and the motion emulation process can be found in IV – VI.

The target vehicles that were measured and used in the ISAR experiments in IV are shown in Fig. 3.1. Fig. 3.2 illustrates the motion emulation process. In Fig. 3.2a, the intensity of a 20 degree CPI of the range-compressed turntable data of object (d) in Fig. 3.1 before the motion emulation is shown. As seen from the signal intensity after motion emulation in Fig. 3.2b, the response is shifted in range and stretched in slow-time due to the emulated motions. In all of the ISAR experiments of this thesis, we considered imaging vehicles moving on the ground. However, the techniques presented in the thesis are not restricted only to imaging objects moving on the ground, but they are equally

applicable to imaging air- or maritime objects as well.

3.2 Range alignment

In range alignment, the slow-time-dependent radial distance r_0 between the center of the object and the radar is estimated. As discussed in Chapter 2, several existing range alignment algorithms are based on mathematical optimization [14–16, 19, 119]. Range alignment provides a coarse estimate of the translational motion of the object, because it can only compensate for translational motions that are comparable in magnitude to the range resolution. However, the accuracy of the result has to be almost the same as the range resolution to guarantee a good result in the subsequent ISAR processing.

In IV–V, two significant improvements were proposed for the range alignment procedure. The first improvement is to combine the loss functions used in [15, 16, 119] to take full advantage of their complementary nature. The second improvement concerns the optimization procedure; we solved it by using a carefully selected initial guess and by using first and second order numerical optimization by deriving expressions for the partial derivatives of the loss function.

To overcome the limitations of the common loss functions (2.8)–(2.9), we proposed combining them as

$$L_{RA} = H(L_1, \ldots, L_K), \tag{3.1}$$

where $H : \mathbb{R}^K \to \mathbb{R}$ is a function that combines the good qualities of the different loss functions. Using (3.1) as the loss function is motivated by the fact that (2.8) works ideally when the object does not rotate significantly during the CPI. On the other hand, (2.9) works well even if the shape of the range profile changes during the CPI due to significant object rotation. Let us denote the negative contrast of the sum envelope as L_1, the entropy as L_2 and the mean squared envelope difference as L_3. As an example, we can choose $H(L_1, L_3) = -L_3/L_1$. For the entropy of the sum envelope either $H(L_1, L_3) = L_1 + L_3$ or $H(L_1, L_3) = L_1 L_3$ are possible choices. In V, a large number of possibilities for H were tested. The only constraint in choosing H is that it should be continuously differentiable. This restriction stems from the optimization algorithm used to solve the minimization problem.

The next proposed improvement is to use an initial guess for the optimization algorithm. As the rate of convergence of numerical optimization can depend significantly on the accuracy of the starting point, it makes sense to use extra effort in finding a good initial guess. We used the computationally very efficient maximum correlation method [133] for this purpose. In other words, the initial guess is obtained as

$$\eta_m^0 = \arg\max_r \left\{ |ss(r, t_0)| \star_r |ss(r, t_m)| \right\}. \tag{3.2}$$

The maximum correlation method is used to produce an initial guess, which is accurate enough to turn the global optimization problem into a local problem. In general, the loss function is non-convex, as was shown in V. Using a parametric model for the range shift can be justified, because it is unlikely that the imaged objects will exhibit rapid random motions between adjacent slow-time samples. The parametric model also helps reduce the computational burden of the optimization by reducing the number of unknown parameters. The parametric model expresses the range shifts in the form

$$\eta_m = \sum_{j=0}^{J-1} a_j f_j(t_m), \tag{3.3}$$

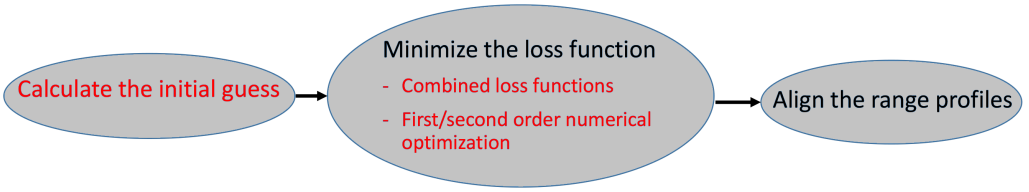

Figure 3.3: The range alignment algorithm estimates the range shifts needed to align the range profiles by minimizing the loss function using a carefully selected initial guess. The proposed modifications to the well-established procedure are highlighted.

where $\{f_j\}_{j=1,\ldots,J}$ is a set of J basis functions, and a_j are their coefficients.

To carry out the minimization of the loss function (3.1) in a computationally efficient manner, we proposed a local optimization approach based on the gradient and the Hessian of the loss function in IV–V. The first and second order partial derivatives of the loss function (3.1) can be expressed as

$$\frac{\partial L_{RA}}{\partial \eta_m} = \sum_k \frac{\partial H}{\partial L_k} \frac{\partial L_k}{\partial \eta_m} \tag{3.4}$$

and

$$\frac{\partial^2 L_{RA}}{\partial \eta_m \partial \eta_n} = \sum_k \left(\sum_l \frac{\partial^2 H}{\partial L_l \partial L_k} \frac{\partial L_l}{\partial \eta_m} \frac{\partial L_k}{\partial \eta_n} + \frac{\partial H}{\partial L_k} \frac{\partial^2 L_k}{\partial \eta_m \partial \eta_n} \right). \tag{3.5}$$

The results (3.4)–(3.5) can be used to obtain the parametric versions of the partial derivatives by using the chain rule. This yields

$$\frac{\partial L_{RA}}{\partial a_l} = \sum_m \frac{\partial L_{RA}}{\partial \eta_m} \frac{\partial \eta_m}{\partial a_l} = \sum_m f_l(t_m) \frac{\partial L_{RA}}{\partial \eta_m} \tag{3.6}$$

and

$$\frac{\partial^2 L_{RA}}{\partial a_k \partial a_l} = \sum_m \sum_n f_k(t_m) f_l(t_n) \frac{\partial^2 L_{RA}}{\partial \eta_m \partial \eta_n}. \tag{3.7}$$

The results (3.6)–(3.7) were used to implement the steepest descent and Newton-Raphson algorithms in IV and V, respectively. The Newton-Raphson algorithm is based on the iterative update equation

$$\boldsymbol{\eta}^{j+1} = \boldsymbol{\eta}^j - (\boldsymbol{H}^j)^{-1} \boldsymbol{g}^j, \tag{3.8}$$

where j is the number of iteration, $\boldsymbol{H}_{mn} = \partial^2 L_{RA} / \partial \eta_m \partial \eta_n$ is the (m,n)-component of the Hessian, and $\boldsymbol{g}_m = \partial L_{RA} / \partial \eta_m$ is the mth component of the gradient. Once the optimization algorithm locates the value of $\boldsymbol{\eta}$ that minimizes L_{RA}, it is used to align the range profiles utilizing (2.7). The basic principle of the range alignment algorithm is illustrated in the flowchart of Fig. 3.3.

In IV and V, the proposed improvements were shown to increase the computational efficiency of range alignment by an order of magnitude compared to the benchmark algorithms. In the numerical experiments of IV and V, the ground truth of the emulated translational motions was known. Thus, the estimation performance could be evaluated by calculating the standard deviations σ_e of the residual estimation error. As another performance metric, the contrast of the ISAR image after applying PGA and keystone

Table 3.1: Estimation accuracy of range alignment and the resulting ISAR image contrast for 14 different loss functions H (L_1, L_2, and L_3 are the benchmarks). The results are reproduced from V.

Loss function H	Mean residual error $\langle\sigma_e\rangle[m]$	Image contrast
L_1	0.1551	17.9824
L_2	0.1734	18.4888
L_3	0.2209	16.6655
$-L_3/L_1$	0.1115	18.6123
$-L_2/L_1$	0.1072	18.8486
L_2L_3	0.1113	18.9444
$-1/L_1+L_3$	0.0920	18.6500
$-1/L_1+L_2$	0.0983	18.9800
L_3+L_2	0.1081	19.1103
$-1/L_1+L_2+L_3$	0.0983	18.9762
$-(1/L_1)\,(L_2+L_3)$	0.0982	18.9756
$L_3\,(-1/L_1+L_2)$	0.1072	18.8483
$L_2\,(-1/L_1+L_3)$	0.1117	18.9810
$-L_2L_3/L_1$	0.1072	18.9335

formatting was calculated. In the performed tests, 20 different target trajectories were considered. The mean values of these results for 14 different choices of H are shown in Table 3.1. The benchmarks are L_1, L_2, and L_3. As seen from the results in Table 3.1, the estimation accuracy of the new loss functions (3.1) was as much as 35 percent higher than the accuracy of the benchmarks. Noteworthy, the improved performance was achieved for a very high range resolution (10 cm) and for a significant object rotation (25 degrees during the CPI). The increased estimation accuracy manifested itself as an improvement of about 7 percent in the ISAR image contrast value.

In I, we used a heuristic optimization algorithm to solve the minimization problem. DE was used with a spline polynomial parametrization for the range shifts. The first and second order optimization approaches in IV and V are more sensitive to the energy scale of the signal (which can cause large differences in the values of the different loss functions) and scale differences in the coefficients of the polynomial model. However, as demonstrated in V, the computational burden of the heuristic optimization approach in I is approximately two orders of magnitude higher. The algorithms proposed in IV and V solve the range alignment in a matter of seconds, while the DE approach takes up to a few minutes even with a relatively accurate initial guess.

3.3 Time window optimization

The purpose of time window optimization is to choose an optimal CPI from the available data for the ISAR image reconstruction. This can be achieved by locating a slow-time window during which the object movement is as smooth as possible. To determine this slow-time window an optimization problem with a suitable loss function needs to be defined. The most straightforward way is to use the negative ISAR image contrast, as was done in [43]. In this approach, the ISAR image reconstruction is done by assuming the simple signal model (2.12) and using a one-dimensional Fourier transform. However, this approach has its drawbacks. Because this procedure takes place after range alignment, the residual phase error ϕ_e can cause the image to be significantly out of focus. Also,

scatterer RCM due to the rotational motion needs to be taken into account when a very high resolution image is the desired outcome.

To deal with the two aforementioned problems, we proposed two modifications for the time window optimization procedure in IV. As in [43], the contrast of the intensity-normalized ISAR image is used as the quality measure to determine the optimal length T and location t_c for the CPI. To deal with the scatterer RCM, keystone formatting [44,45] is used prior to the image reconstruction. Additionally, autofocus using the PGA algorithm [30,32,118] is applied to remove the spatially invariant phase errors ϕ_e to obtain a well-focused image. A drawback of this approach is that the modifications entail an increased computational burden for the time window optimization. The increased computation is countered by suitably modifying the PGA algorithm, using a sub-optimal interpolation in the keystone formatting, and using a local numerical optimization algorithm in solving the minimization problem.

In II, we proposed a method for determining the optimal CPI for keystone formatting without having to reconstruct the ISAR image. The optimization procedure of this approach is based on the same loss functions utilizing the sum envelope of range-compressed signal as in the range alignment problem. In II, time window optimization based on the image contrast was applied after this operation. Thus, the formulation presented in IV combines the two different parts of the algorithm that were used in II, which results in a computationally more efficient algorithm.

Fig. 3.4 illustrates the loss function evaluation process in the time window optimization. The highlighted motion compensation steps are described next. An ISAR image sS from a CPI of length T located around t_c is obtained as

$$sS(t_c, T; x, y) = \mathcal{F}_{t\to y}\left\{\Pi\left(\frac{t-t_c}{T}\right) ss(x,t)\right\}. \tag{3.9}$$

Before evaluating the contrast of the image (3.9), PGA and keystone formatting are applied to remove both spatially invariant and spatially variant defocusing effects. First, the residual phase errors ϕ_e are compensated for by using PGA, because the non-linear part of ϕ_e affects the result of keystone formatting in an undesirable way. The standard PGA algorithm is used with a simple modification to reduce the need for multiple iterations. Namely, the circular shifting operation of PGA is replaced by a more efficient procedure. The method was originally proposed in [134]. It removes the phase offsets from the phase derivative estimates of different range bins by subtracting the time average of the phase derivative from the estimate in each range bin. This results in a more accurate removal of the offsets than the circular shifting operation, especially if the image (3.9) is severely defocused. This increased accuracy enhances the estimation performance in the first iterations, which speeds up the convergence of the PGA. This causes significant computational savings in the time window optimization, because PGA is used every time the loss function is evaluated. The details of this process are described fully in IV.

Only one iteration of PGA is applied in the time window optimization algorithm to reduce the computational cost. The procedure described above makes sure that we get the best possible result out of this single iteration. Once PGA produces an estimate $\widehat{\phi_e}$ for the phase errors, the range-compressed signal is phase-corrected according to

$$ss_c(t_c, T; x, t) = \Pi\left(\frac{t-t_c}{T}\right) ss(x,t) e^{-i\hat{\phi}_e(t)}. \tag{3.10}$$

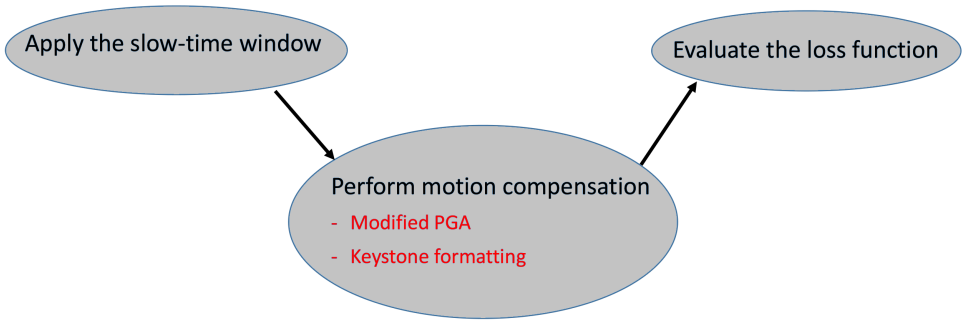

Figure 3.4: The loss value in the time window optimization is calculated after motion compensation is performed for the time-windowed signal. The proposed motion compensation steps are highlighted.

Table 3.2: Optimal window lengths (T), image contrast values, and relative computational speeds for different motion compensation strategies in the time-window optimization. The first row (COA) represents the benchmark algorithm [43].

Motion compensation	T [samples]	Image contrast	Relative speed
COA	336	77.57	1
COA + Keystone formatting	352	82.55	0.79
PGA	320	90.30	7.5
PGA + Keystone formatting	363	99.89	4.8

Next, keystone formatting (denoted as $\mathcal{K}$) is applied to remove the linear RCM of the scatterers caused by the object rotation as

$$ss_{\mathcal{K}}(t_c, T; x, \tau) = \mathcal{F}^{-1}_{k_x \to x}\left\{\mathcal{K}_{t\to\tau}\left\{Ss_c(k_x, t)\right\}\right\}. \tag{3.11}$$

The intensity-normalized intensity ISAR image is obtained by using (3.11) as

$$\widehat{I}(t_c, T; x, y) = \frac{I(t_c, T; x, y)}{\iint_{-\infty}^{\infty} I(t_c, T; x', y')dx'dy'}, \tag{3.12}$$

where $I(t_c, T; x, y) = |sS_{\mathcal{K}}(t_c, T; x, y)|^2$. The loss function can be defined in a similar manner as in COA (see (2.15)); the only difference is that now it only depends on two variables (T and t_c). The time window optimization is carried out by minimizing this loss function using a black-box local numerical optimization algorithm. Assuming that the PRF is high compared to the time scale in which the motion of the object changes significantly the loss function behaves relatively smoothly. It should be noted that the loss function is not convex, and thus a local optimization approach can lead to a sub-optimal solution.

In the experimental section of IV, the result of the method described above was compared to the maximum contrast time window optimization procedure proposed in [43]. The point of this comparison was to illustrate the effect of the motion compensation strategy included in the loss evaluation. In the benchmark [43], only COA is performed prior to evaluating the image contrast. To ensure that the comparison was done in a meaningful way, a simple coordinate descent optimization algorithm was used in solving the optimization

problems. The results of the study are shown in Table 3.2. They show that our strategy of using PGA and keystone formatting is computationally more efficient than the benchmark and it produces the best image contrast value. The inclusion of the keystone formatting increased the contrast by 6 – 10 percent compared to both benchmarks, COA and PGA. Noteworthy, our strategy of using PGA and keystone formatting was almost five times faster than the benchmark method [43] based on COA alone.

3.4 Autofocus

PGA is used as the autofocus algorithm in the time window optimization due to its simplicity and computational efficiency compared to other algorithms. COA has also been demonstrated to produce very good results in both ISAR and spotlight mode SAR autofocus [13,14,17,22,25,27]. It is especially effective in ISAR imaging, since the objects typically exhibit some strong point-like reflections. The loss functions used in COA are very sensitive to the degree of focus of these point-like scatterers. In IV, a theoretical result was derived for the COA, which makes it possible to improve its computational efficiency. We argued that when the phase errors are small in magnitude, COA can be applied in a highly computationally efficient manner. The underlying reason for this stems from the fact that the loss function can be regarded as separable when the phase error estimates are small in magnitude. Under this assumption, COA is reduced into solving a series of one-dimensional optimization problems.

In [22,25], an expression for the gradient of the loss function (2.15) was derived. Expressing it in terms of (2.15) we have

$$\frac{\partial L}{\partial \boldsymbol{\phi}} = \iint_{-\infty}^{\infty} \frac{\partial \Psi(I(\boldsymbol{\phi}; x, y))}{\partial I} \frac{\partial I(\boldsymbol{\phi}; x, y)}{\partial \boldsymbol{\phi}} dxdy. \tag{3.13}$$

Assuming that ψ is twice continuously differentiable, we can take this process one step further to yield

$$\frac{\partial^2 L}{\partial \phi_m \partial \phi_n} = \iint_{-\infty}^{\infty} \left(\frac{\partial^2 \Psi}{\partial I^2} \frac{\partial I}{\partial \phi_m} \frac{\partial I}{\partial \phi_n} + \frac{\partial \Psi}{\partial I} \frac{\partial^2 I}{\partial \phi_m \partial \phi_n} \right) dxdy \tag{3.14}$$

for the second order partial derivatives. In IV, the result (3.14) is further refined to yield an expression in terms of the range-compressed signal ss. Using the full Newton-Raphson method for COA is not feasible for two important reasons. The first is the computational complexity of evaluating and inverting the Hessian (3.14). The other is the fact that the Hessian is not positive definite and is close to singular when we are far away from the minimum. If the loss function is separable (as it is for small phase errors [17]), the essential information is contained in the diagonal elements of the Hessian (3.14). This observation was used to implement the one-dimensional secant method for each phase error component separately, leading to a computationally efficient COA implementation in IV.

3.5 Cross-range scaling

In IV, a combination of the rotation correlation [68] and polar mapping [69] methods was proposed for the cross-range scaling problem. The motivation for combining their good qualities was two-fold: the unknown center of rotation in the rotation correlation method and the computationally demanding two-dimensional interpolation of the polar mapping

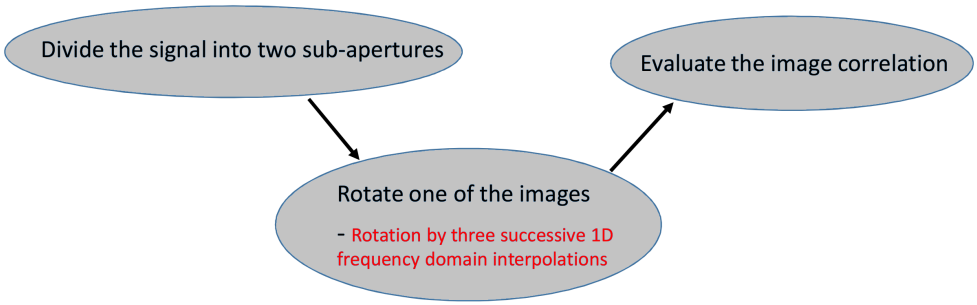

Figure 3.5: The cross-range scaling algorithm estimates the angular shift between two sub-aperture ISAR images. The highlighted method for image rotation in the frequency domain was proposed.

method. As is done in the polar mapping method, the combined algorithm utilizes the fact that the rotation can be carried out in the spatial frequency domain without knowing the location of the center of rotation in the spatial domain. The underlying idea of both methods is to estimate the angular shift between two sub-aperture ISAR images that are made from different parts of the signal.

As discussed in Chapter 2, the two sub-aperture images are rotated and scaled versions of each other. Mathematically, the sub-aperture signals in the two-dimensional spatial frequency domain are related by

$$G_1(k_x, k_y) = \mathcal{R}(\theta(t_{c1}) - \theta(t_{c2}))G_2(k_x, k_y), \tag{3.15}$$

where $\mathcal{R}(\theta)$ denotes the operation which rotates a function by the angle θ and

$$G_i(k_x, k_y) = \mathcal{F}_{x \to k_x} \left\{ \Pi \left(\frac{\theta - \theta_{ci}}{\Theta} \right) ss(x, \theta) \right\}, \tag{3.16}$$

where θ_{ci} (i=1,2) are the aspect angle (slow-time) centers of the sub-apertures and the aspect angle variable has been substituted for the cross-range spatial frequency $k_y = 2k_r \sin\theta$. By making an estimate for the angular shift $\hat{\theta}$ between the images G_1 and G_2, an estimate for the sample spacing in the k_y variable can be obtained. This is required to rotate the image correctly. Using this estimate, the Fourier transform G_2 is rotated by the angle estimate $\hat{\theta}$. The rotation is carried out by decomposing it into a series of three shears, which can all be implemented using one-dimensional operations. This is the advantage compared to the polar mapping method, which needs a two dimensional interpolation in the frequency domain. The decomposition has originally been developed for image processing applications [135, 136]. The rotated spectrum is inverse Fourier transformed to obtain the rotated image as

$$g_2(\hat{\theta}, x, y) = \mathcal{F}^{-1}_{k_x \to x} \left\{ \mathcal{F}^{-1}_{k_y \to y} \left\{ \mathcal{R}(\hat{\theta}) G_2(k_x, k_y) \right\} \right\}. \tag{3.17}$$

The loss function is the intensity correlation between the sub-aperture images, which is defined as

$$L_{CR}(\hat{\theta}) = -\iint_{-\infty}^{\infty} |g_1(x, y)|^2 |g_2(\widehat{\theta}, x, y)|^2 dx dy. \tag{3.18}$$

Minimizing (3.18) produces an estimate for the angular shift between the sub-aperture images, which can be used to deduce the cross-range scale of the ISAR image using (2.25). The procedure used to evaluate the loss function is illustrated in the diagram of Fig. 3.5. This formulation for the cross-range scaling is valid when the sub-aperture images are formed from relatively short CPIs during which the object rotates smoothly. Compared to the polar mapping method, neither a two-dimensional resampling or a complex iterative procedure is needed. This yields a lower number of operations even for high-quality interpolators, resulting in computational savings. In the numerical experiments of IV, the algorithm was empirically validated to yield a low discrepancy of 4 – 8 percent in terms of the true dimension of the imaged objects.

3.6 Time-frequency-based image reconstruction

As discussed in Chapter 2, TFRs can be used to reduce the effect of spatially variant defocusing caused by the rotational motion of the object. In this approach, the matched filtering is performed by replacing the Fourier transform by a suitable high-resolution TFR. The time-frequency-based image reconstruction has been demonstrated to be effective using various TFRs [46, 49 – 51, 54, 57 – 59, 137]. A particularly effective choice for the TFR is the S-method [138]. This choice is motivated by its simplicity and computational efficiency. The S-method was shown to surpass the conventional Fourier transform-based range-Doppler image reconstruction in [59] under complicated target motions during the CPI. The S-method is capable of compensating high-order phase terms due to both translational and rotational motions of the target.

The S-method belongs to the class of quadratic TFRs, and it can thus be formulated using the Cohen's class (2.21). Using the definition of the S-method, the ISAR image reconstruction is achieved by evaluating

$$SM(r, y, t) = \int_{-\infty}^{\infty} P(\nu) sS(r, y + \nu, t) sS^*(r, y - \nu, t) d\nu, \tag{3.19}$$

where

$$sS(r, y, t) = \mathcal{F}_{\tau \to y} \left\{ w(\tau - t) ss(r, \tau) \right\} \tag{3.20}$$

is the Short Time Fourier Transform (STFT) of the range-compressed signal obtained by using a window function w. The window of the STFT can simply be a rectangular window, whose length has been determined by the time window optimization procedure. The kernel function of the S-method can be shown to be

$$\Phi(t, y) = 2\mathcal{F}^{-1}_{\nu \to 2t} \left\{ P(\nu) \right\} \mathcal{F}_{\tau \to y} \left\{ w(t + \frac{\tau}{2}) w(t - \frac{\tau}{2}) \right\}. \tag{3.21}$$

In (3.19), the window function P limits the range of integration in (3.19). By choosing the length of this window appropriately, the oscillating cross-terms in the TFR can be suppressed. A simple and effective choice is to use a rectangular window $P(y) = \Pi(y/\Omega)$ of length Ω.

An optimal choice for the kernel function Φ of the TFR depends on the nature of the motion of the non-cooperative object. In II and IV we proposed an optimization procedure for determining the optimal window function for the S-method. Essentially, the time window optimization procedure described above determines an optimal window for the STFT. The next step is determine the optimal S-method window P to be used in (3.19). This window is determined by maximizing the contrast of the intensity normalized ISAR

Table 3.3: Comparison of image contrast values for the range-Doppler image without the S-method modification ($\Omega = 0$), the S-method image with a range-independent window Ω (benchmark), and the S-method image with a range-dependent window $\Omega(r)$ (proposed algorithm).

S-method window type	Image contrast
$\Omega = 0$	99.89
Range-independent Ω	121.34
Range-dependent $\Omega = \Omega(r)$	128.73

image. The image intensities have to be normalized to make the usual COA loss functions of the type (2.15) applicable for this problem. The optimization procedure proposed in IV uses a range-dependent window in the S-method. Mathematically, this is represented as

$$SM(r, y, t) = \int_{-\Omega(r)/2}^{\Omega(r)/2} sS(r, y + \nu, t) sS^*(r, y - \nu, t) d\nu. \tag{3.22}$$

Using (3.22), the intensity normalized image and the loss function based on the image contrast can be formulated analogously to (3.12) and (2.15). The minimization is carried out for each range bin separately, which means that the loss function is the contrast of the cross-range profile instead of the entire image.

The contrast optimization approach can be motivated by the following observations: At first, increasing the length Ω of the integration window sharpens the image in the cross-range direction. At some optimal point, the best possible resolution without cross-terms is achieved, and the image contrast is maximized. Increasing the length Ω beyond this optimal point causes cross-terms to appear between scatterers in the image. This manifests itself as image blurring and thus decreases the image contrast. Thus, the contrast optimization leads to a compromise between enhanced cross-range resolution and cross-terms in the ISAR image. Additionally, the optimal length for Ω will be relatively short when several scatterers occupy the same range bin. This means that the computational effort required for the optimization will be small. In practice, the optimization starts from a window length of zero samples and increases the length until the minimum of the loss function is reached.

The proposed optimization procedure was tested experimentally in IV. Table 3.3 shows the image contrast values for $\Omega = 0$ (STFT-based image), a fixed range-independent window Ω, and a range-dependent window $\Omega(r)$. Using a range-dependent window increased the contrast by six percent compared to a fixed range-independent window. Compared to the STFT-based image the contrast increased as much as 30 percent, which can be attributed to the challenging motion compensation scenarios including non-uniform rotational motion.

A benefit of using the S-method is that only a single time sample (ISAR image frame) of the TFR can be obtained very computationally efficiently. For example in IV we chose this time sample to be the center of the CPI determined by the time-window optimization procedure. After the ISAR image has been formed using a TFR, it is possible to apply the time-frequency reassignment procedure [139] to further increase the image contrast. Its use in ISAR imaging has been demonstrated with experimental data in [140, 141]. We applied it for the S-method in II and demonstrated the increase in image contrast in quantitative terms. The reassignment operation can result in improved image contrast, because it can further compress the amplitude envelopes of the scatterer responses in the

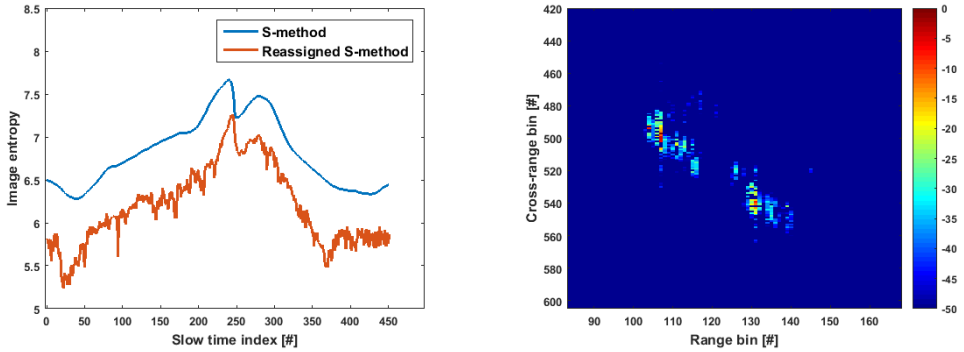

(a) Image entropy. **(b)** Reassigned S-method ISAR image.

Figure 3.6: The reassignment operation lowers the image entropy in (a) and improves the image contrast. The strong scattering centers of the object can clearly be distinguished from the reassigned ISAR image (b). The figures are reproduced from II.

cross-range direction. However, it can only do so for points that can already be resolved in the original ISAR image. The reassignment is mathematically represented as

$$RSM(r,y,t) = \iint_{-\infty}^{\infty} SM(r,y',t')\delta(t-\hat{t}(r,y',t'))\delta(y-\hat{y}(r,y',t'))dt'dy', \tag{3.23}$$

where $\hat{t}$ and $\hat{y}$ are the reassigned slow-time and cross-range values. For the S-method, they can be obtained very efficiently using the results derived in [142].

The key experimental results of II are illustrated in Fig. 3.6. As seen from Fig. 3.6a, the reassignment operation decreases the image entropy and thus increases the ISAR image contrast by approximately 8 percent on average. The scatterer responses in the reassigned image 3.6b are very concentrated. The corresponding S-method image without reassignment was shown previously in Fig. 2.4b. Visual comparison confirms that the reassignment squeezes the amplitude envelopes of the scatterer responses producing a sharper image of the object.

3.7 Discussion

Fig. 3.7 presents a summary of the entire ISAR processing chain in the form of a flowchart. The proposed improvements to each step have been described in the previous sections. In IV, we demonstrated the ISAR processing chain of Fig. 3.7 including our improvements for each step using experimental radar data. Using a standard laptop computer with MATLAB, the processing took about 25 seconds on average. The time window optimization was the computationally most demanding part of the algorithm taking up almost half of the total computational effort. We compared the performance of our algorithm with the well-established approach consisting of the processing steps of Fig. 3.7 without our improvements. The computation time for this approach averaged at 45 seconds. Considering this result, the proposed improvements resulted in increased computational efficiency in the ISAR processing overall. A noteworthy contribution of IV was to combine the state-of-the-art ISAR processing steps into a well-defined total ISAR algorithm as depicted in Fig. 3.7. The ISAR literature contains a lot of different

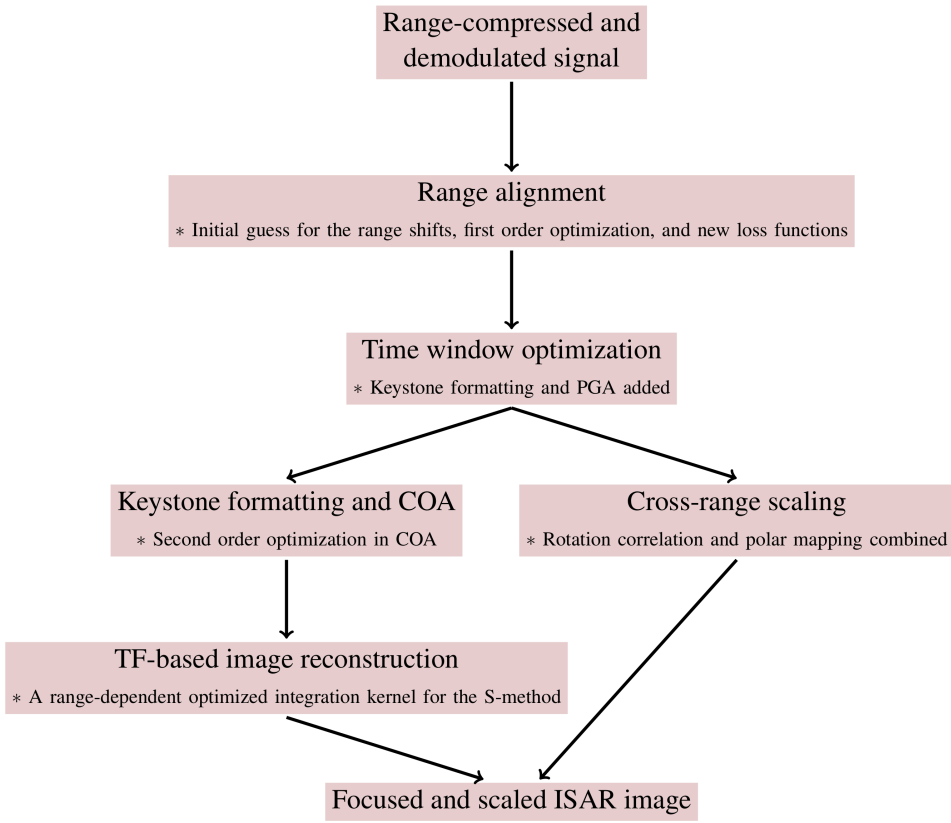

Figure 3.7: State-of-the-art ISAR processing can be decomposed into algorithmic steps as shown here. The proposed improvements, which lead to increased estimation performance and computational efficiency, are indicated below the steps. The flow-chart is reproduced from IV.

methods but at the moment lacked a complete state-of-the-art description of the entire motion compensation and image reconstruction process.

The improved imaging result of the proposed optimization-based ISAR processing is visualized in Fig. 3.8. Fig. 3.8a is the result of the well-established ISAR processing while Fig. 3.8b shows the result of our algorithm. The ISAR images are of the Ford Focus depicted in Fig. 3.1a. In this case, a notable 50 percent increase in the image contrast is obtained for this trajectory realization. Taking into account all the experiments in IV, the image contrast increased by 28 percent on average. Visual inspection of the images in Fig. 3.8 reveals that significantly less spatially variant blurring occurs in Fig. 3.8b.

The methods described in this Chapter provide a way to perform blind data-driven motion compensation without making any assumptions or utilizing a priori information about the target motion dynamics. They improve the ISAR imaging performance especially in situations where the non-cooperative object exhibits changing translational and rotational motions during the ISAR data acquisition. As an attractive quality, the proposed methods reduce to well-established processing methods if the object moves very smoothly and the quality of the image cannot be improved by additional motion compensation.

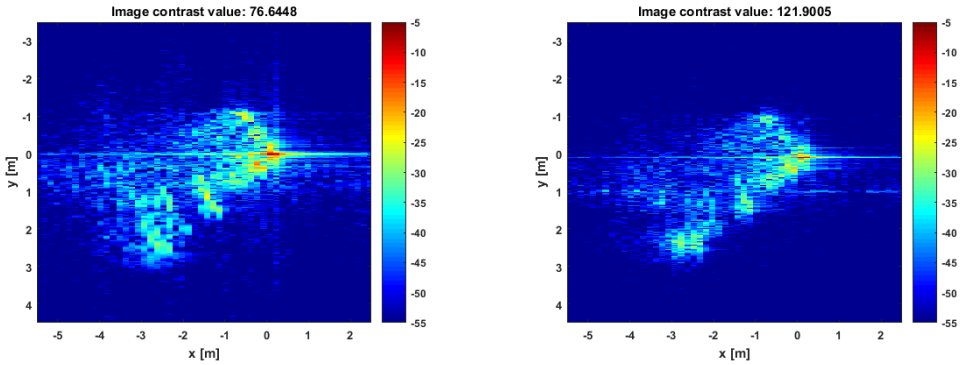

(a) Result of well-established ISAR processing.

(b) Result of proposed ISAR processing.

Figure 3.8: Comparison of ISAR images for well-established ISAR processing in (a) and our improved ISAR processing (b) reveals increased image contrast and reduced spatially variant defocusing. The figure is reproduced from IV.

The purpose of ISAR imaging usually is to provide target signatures for recognition purposes. The focused ISAR images obtained with the proposed optimization-based ISAR processing contain a lot of useful information for target recognition applications. The quality of motion compensation is very important, because target recognition requires well-focused images. This is because the the size, the shape, and the dominant scatterers of the objects need to be correctly resolved in the images for successful image exploitation. In many current target recognition approaches, a major challenge is related to the unknown motion of the imaged object, which causes the image to be out of focus and the orientation of the object to be unknown. An important future direction of this work is to evaluate the effect the increased image contrast and resolution have on the recognition capability.

A possible way to further increase the computational efficiency of the proposed ISAR processing would be to incorporate a priori knowledge about the target dynamics and trajectory into the estimation process. In practical applications, such information is often available because of (low-resolution) target tracking and because the expected target types are known (air, ground, or maritime targets). The information obtained from target tracking could be used for coarse initial motion compensation or as initial guesses in the proposed optimization approaches. The expected target types and their associated kinematic models could be used to help in choosing appropriate models for the optimized motion parameters, which can help in avoiding over-parameterization.

4 Computationally efficient time domain image reconstruction

As discussed in Chapter 2, conventional methods for image reconstruction in both non-cooperative ISAR and MSAR rely on several approximations. Computationally efficient algorithms come at a cost of degraded image quality and limited algorithm applicability. Time domain image reconstruction algorithms offer an attractive alternative by removing these limitations. However, they are not yet in full use by operational SAR and ISAR systems due to their high computational burden. Due to the constantly increasing computational power, this is about to change in the near future. The situation calls for computationally efficient and reliable motion compensation and image reconstruction algorithms capable of delivering increased imaging performance.

In I, III, and VI we proposed time domain image reconstruction algorithms for ISAR and MSAR. The proposed time domain imaging approach to non-cooperative ISAR is analyzed in Section 4.1. A comparison with the optimization-based ISAR processing of Chapter 3 is performed using the data and motion emulation process described in Section 3.1. Section 4.2 presents the proposed MSAR time domain algorithms and presents simulated results associated with them. The findings for both applications of time domain image reconstruction (ISAR and MSAR) are summarized and discussed in Section 4.3.

4.1 Back-projection algorithm for non-cooperative ISAR

As the spatial resolution becomes extremely high (≈ 10 cm) in non-cooperative ISAR imaging, the practice of dividing the motion compensation into several consecutive steps as in Fig. 3.7 is no longer an ideal approach. This is because many of the approximations used to motivate and derive the approaches presented in Chapter 3 start to break down. For example, the one-dimensional phase error assumption in autofocus and the linear RCM assumption in keystone formatting are no longer valid for extremely fine range resolutions and long CPIs. In the context of time domain image reconstruction using back-projection (2.27), it would be more feasible to estimate the translation and the rotation simultaneously. To achieve this, we proposed a contrast optimization approach for back-projection image reconstruction in non-cooperative ISAR in VI. The algorithm is based on a computationally efficient first order optimization procedure where the motion compensation algorithms of Chapter 3 are used to provide accurate initial guesses for the motion parameters of the object.

Contrast optimization approach

The idea behind our time domain ISAR imaging approach is very simple: We estimate the motion parameters by maximizing the image contrast. Mathematically, the problem is formulated as

$$\{\boldsymbol{\eta}^\star, \boldsymbol{\theta}^\star\} = \arg\min L(\boldsymbol{\eta}, \boldsymbol{\theta}), \tag{4.1}$$

where the loss function is formulated analogously to (2.15). However, compared to the conventional COA approach considered in Chapter 3, there exists a number of difficulties. Most importantly, we can't assume that the translational motion is constrained within a range resolution cell. Because of this, the translation cannot be compensated for by a one-dimensional phase correction as in conventional autofocus. To avoid computationally intensive global optimization, we proposed using the range alignment and cross-range scaling methods described in Chapter 3 to provide initial guesses for the optimization algorithm. The initial guesses are used to increase the probability that the optimization algorithm converges rapidly to the global optimum solution producing a focused ISAR image.

In VI, we showed how to derive expressions for the partial derivatives of the loss function with respect to the unknown motion parameters. Because η and θ are not known a priori, the ISAR image (2.27) depends on them. In other words $\widehat{g} = \widehat{g}(\boldsymbol{\eta}, \boldsymbol{\theta}; x, y)$, where $\boldsymbol{\eta} = [\eta_0 \dots \eta_{M-1}]^T$ and $\boldsymbol{\theta} = [\theta_0 \dots \theta_{M-1}]^T$. The first step of the derivation is equivalent to the COA autofocus case in (3.13). Straightforward differentiation yields

$$\begin{aligned} \frac{\partial L(\boldsymbol{\eta}, \boldsymbol{\theta})}{\partial \boldsymbol{\eta}} &= \iint_{-\infty}^{\infty} \frac{\partial \Psi(I(\boldsymbol{\eta}, \boldsymbol{\theta}; x, y))}{\partial I} \frac{\partial I(\boldsymbol{\eta}, \boldsymbol{\theta}; x, y)}{\partial \boldsymbol{\eta}} dxdy \\ &= 2\Re\left\{ \iint_{-\infty}^{\infty} \frac{\partial \Psi(I(\boldsymbol{\eta}, \boldsymbol{\theta}; x, y))}{\partial I} \frac{\partial \widehat{g}(\boldsymbol{\eta}, \boldsymbol{\theta}; x, y)}{\partial \boldsymbol{\eta}} \widehat{g}^*(\boldsymbol{\eta}.\boldsymbol{\theta}; x, y) dxdy \right\}, \end{aligned} \tag{4.2}$$

where $I = \widehat{g}\widehat{g}^*$. Carrying out the differentiation of the back-projection image amplitude $\widehat{g}$ with respect to η yields

$$\frac{\partial \widehat{g}(\boldsymbol{\eta}, \boldsymbol{\theta}; x_p, y_p)}{\partial \eta_k} = \exp\left[i \frac{4\pi R_p(t_k)}{\lambda} \right] \left[s'(R_p(t_k), t_k) + i \frac{4\pi}{\lambda} s(R_p(t_k), t_k) \right], \tag{4.3}$$

where $s' = \partial s / \partial r$ and $R_p(t_k) = \eta_k + x_p \cos\theta_k + y_p \sin\theta_k$. If we assume that after the range alignment the residual translational motion is constrained within a range resolution cell, then a one-dimensional slow-time-dependent phase correction is enough to compensate for it. We derived the gradient for this simpler case in I. However, the results in (4.2) and (4.3) are a generalization of that result. Importantly, we do not have to assume that the residual translational motions are smaller in magnitude than the range resolution. For the partial derivatives with respect to θ, we have

$$\frac{\partial \widehat{g}(\boldsymbol{\eta}, \boldsymbol{\theta}; x, y)}{\partial \theta_k} = \frac{\partial \widehat{g}(\boldsymbol{\eta}, \boldsymbol{\theta}; x, y)}{\partial \Omega} \frac{\partial \Omega(\boldsymbol{\theta}; x, y)}{\partial \theta_k}, \tag{4.4}$$

where

$$\frac{\partial \Omega(\boldsymbol{\theta}; x, y)}{\partial \theta_k} = y \cos\theta_k - x \sin\theta_k. \tag{4.5}$$

The importance of the results (4.2)–(4.5) comes from the possibility to use them in a first order numerical optimization algorithm. We used the steepest descent method in VI to solve the optimization problem using the derived results (4.2)–(4.5). In the

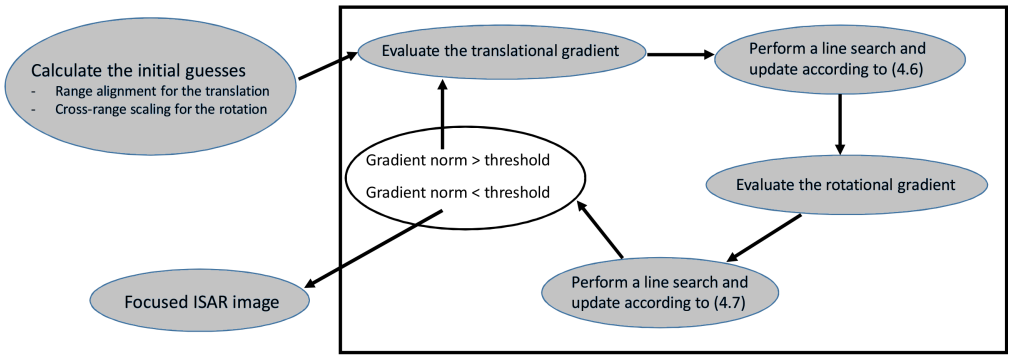

Figure 4.1: The proposed contrast optimization approach for time domain back-projection image reconstruction is based on an iterative first order optimization algorithm, as illustrated in this flowchart.

proposed optimization approach, a single iteration of the algorithm consists of updating the translation according to

$$\boldsymbol{\eta}^{l+1} = \boldsymbol{\eta}^{l} - \varepsilon \frac{\partial L(\boldsymbol{\eta}^{l}, \boldsymbol{\theta}^{l})}{\partial \boldsymbol{\eta}} \tag{4.6}$$

and the rotation according to

$$\boldsymbol{\theta}^{l+1} = \boldsymbol{\theta}^{l} - \zeta \frac{\partial L(\boldsymbol{\eta}^{l+1}, \boldsymbol{\theta}^{l})}{\partial \boldsymbol{\theta}}, \tag{4.7}$$

where the superscript l denotes the number of iteration. The initial estimates $\boldsymbol{\eta}^0$ and $\boldsymbol{\theta}^0$ are obtained by performing the range alignment and cross-range scaling procedures of Chapter 3, as discussed above. The step lengths ε and ζ in (4.6) and (4.7) are obtained by using a line search procedure. A line search corresponds to numerically solving a one-dimensional optimization problem in the negative gradient direction. The iterative process is terminated when the gradient norms become sufficiently small. It is possible, and in most cases even reasonable to end the updating processes (4.6) and (4.7) separately if convergence is reached at different rates. Once the optimization algorithm has terminated, the back-projection image (2.27) is reconstructed with the obtained motion parameters. The optimization algorithm described above is illustrated in the flowchart of Fig. 4.1, where the iterative part of the algorithm is located inside the black rectangle.

Numerical experiments

In VI, we used the experimental setup and motion emulation process described in Section 3.1 of Chapter 3 for evaluating the performance of the proposed time domain focusing algorithm. In short, translational and rotational motions were emulated by shifting the signal in range and resampling in slow-time. The length of the chosen CPI was 20 degrees. The range resolution of the X-band data was 10 cm. In the tests, 20 different motion compensation scenarios were studied. We used $\Psi(I) = -I^2$ as the image sharpness metric in the loss function of the contrast optimization problem.

Knowing the ground truth of the emulated motions makes it possible to use the ideally focused ISAR image as the benchmark in evaluating the performance of the imaging

(a) The measured object.

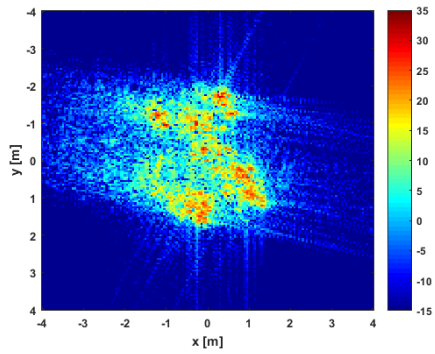

(b) Ideally focused ISAR image of (a).

Figure 4.2: In the performed experiments, the ideally focused imaging result in (b) of the measured object (a) was used as the benchmark. The figure is reproduced from VI.

Table 4.1: Numerical results of the comparative ISAR study. The results are reproduced from VI.

ISAR algorithm	Relative speed	Image contrast	Standard deviation
Ideal back-projection	1	7.65	–
Back-projection with contrast optimization	0.014	8.00	0.50
ISAR algorithm of Chapter 3	0.111	6.71	1.32

algorithm. This ideal imaging result of the measured object in Fig. 4.2a is shown in Fig. 4.2b. As was done for the algorithms of Chapter 3, the image contrast (defined as the ratio between the standard deviation and the mean of the image intensities) was used to measure the imaging performance in quantitative terms.

The results of the performed numerical experiments are listed in Table 4.1. The first row of the table represents the ideal imaging result using back-projection while knowing the ground truth of the motions. The second row lists the results for the proposed contrast optimization approach for time domain back-projection image reconstruction. The third row contains the results of the optimization-based state-of-the-art ISAR processing chain of Chapter 3. The relative computational speed and image contrast values on the second and third rows are the mean values of the 20 different use-cases. The standard deviation of the image contrast values is shown in the last column of Table 4.1.

The higher image contrast value and smaller standard deviation for the proposed time domain focusing algorithm reveal that it was able to provide more consistent results than the ISAR approach of Chapter 3 based on more conventional motion compensation algorithms. However, this increased imaging performance comes at a cost. The computational burden of the time domain focusing algorithm was nearly an order of magnitude greater. In practical terms, the computation time averaged at approximately four minutes when using MATLAB and a standard laptop computer with a 2.60 GHz dual-core processor and 8 GB random access memory.

Figs. 4.3 and 4.4 show the imaging results of the first three (of 20) motion compensation scenarios for the time domain focusing algorithm and the optimization-based ISAR

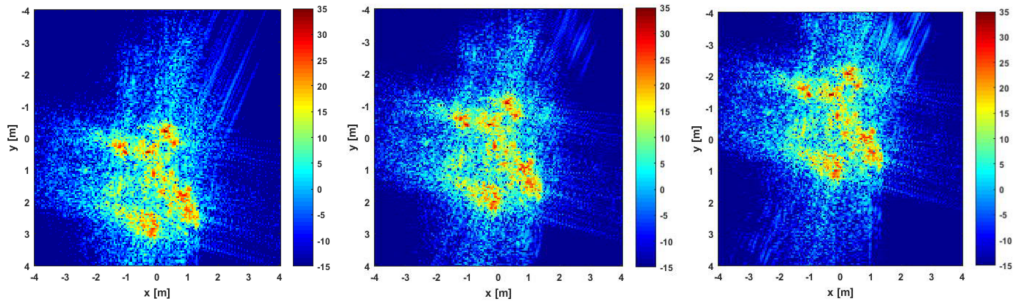

Figure 4.3: The ISAR images after contrast optimization with the proposed time domain focusing algorithm. The degree of focus of the images is consistent, only a shift in cross-range noticeably differentiates the results. The results are reproduced from VI.

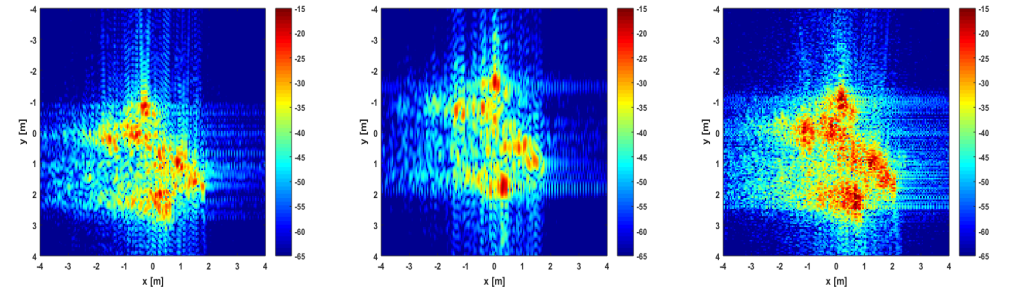

Figure 4.4: The ISAR images obtained by using the optimization-based processing chain of Chapter 3. Image quality varies more compared to the results of the time domain focusing approach in Fig. 4.3 due to the varying degree of non-linearity of the rotational motion. The results are reproduced from VI.

processing of Chapter 3, respectively. The time domain focusing algorithm produces highly focused images, only a shift in cross-range and slightly increased sidelobe intensity levels can be observed from the ISAR images when comparing with the ideal result in Fig. 4.2b. The shift in cross-range is due to a residual linear phase term caused by the translation. Since it only causes a shift but no defocusing, the contrast optimization algorithm is unable to estimate it correctly.

The results in Figs. 4.3 and 4.4 reveal that the time domain focusing algorithm is able to provide more consistent results. The image quality varies more for the optimization-based ISAR processing of Chapter 3. For example, there is a noticeable difference in the image quality in the second experiment. This is mainly caused by the non-linear rotational motion of the object. It causes the time window optimization algorithm to select a much shorter CPI for the image reconstruction than the full 20 degree CPI used in the time domain focusing algorithm. The third motion compensation scenario was not as challenging and resulted in a very high and nearly similar imaging performance for both approaches.

4.2 FFBP algorithms for MSAR

In III, we considered time domain MSAR image reconstruction algorithms based on the multichannel back-projection integral (2.32). The algorithms use the phase center approximation introduced in Chapter 2 and DBF on receive. These approximations together with the FFBP algorithm for SAR image reconstruction were used to develop two computationally efficient time domain image reconstruction algorithms for MSAR in III.

FFBP basics

Without loss of generality, the back-projection integral (2.32) can be partitioned in the slow-time direction. The idea behind the FFBP algorithms [89, 90] is that representing the integration result of a single sub-aperture requires far less resolution elements than the final full resolution image. First, sub-aperture images with coarse resolution are reconstructed on a polar grid with a large spacing in the angular direction. Then, the sub-aperture images are recursively upsampled, interpolated and combined to yield the final image with full resolution. This approach significantly reduces the required number of operations compared to the direct back-projection algorithm.

Since the range-compressed signal has high resolution in the radial range direction, the PTR in the coarse resolution sub-aperture images will be smeared in both (Cartesian) x- and y-directions. Due to this, the sub-aperture images in FFBP have to be represented in a local polar coordinate system, where the radial coordinate is the radial distance measured from the center of the sub-aperture and the angular coordinate is the angle between the radar flight track and the line of sight to the resolution element [89]. In the local polar coordinate system, lines of constant range are straight horizontal lines. This means that the PTR will have high resolution in the radial range direction and coarse resolution in the angular direction. Thus, the resolution element spacing in the angular direction can be chosen to be very coarse in the first stages of the algorithm, which significantly reduces the number of arithmetic operations required in the image reconstruction.

Proposed reconstruction algorithms

The back-projection integral (2.32) can be approximated as

$$\hat{g}(\boldsymbol{r}) = \int_{-\infty}^{\infty} ss(r_n(\boldsymbol{r}; y_n), y_n) e^{i2k_c r_n(\boldsymbol{r}; y_n)} dy_n. \tag{4.8}$$

The integration variable y_n denotes the cross-range location of the approximated monostatic sample positions, which are obtained using the phase center approximation. Essentially, the summation of the n receiver signals at each slow-time instant correspond to additional samples in the along-track direction. The result in (4.8) corresponds to conventional monostatic SAR imaging; it allows a straightforward implementation of the FFBP algorithm. The only extra effort in computation comes from calculating the radial distances $\boldsymbol{r}_n$ between the image pixels and the sample positions for the additional along-track samples.

The ULA system and the recorded multichannel signal can be used to perform DBF on receive. In III, we used phase-shift beamforming of the MSAR signal to obtain a computationally efficient image reconstruction algorithm. In phase-shift beamforming,

the antenna pattern of the ULA is steered to direction β by summing the phase-adjusted receiver signals as

$$ss(r,t) = \sum_{n=0}^{N-1} w(n) sss(n,r,t) \exp\left(i\frac{2\pi}{\lambda_c} nd \sin\beta\right), \tag{4.9}$$

where w is a window function used to control the sidelobe levels of the antenna pattern. The phase-shift beamforming (4.9) is based on a plane-wave approximation. In our reconstruction technique, the beam is steered to continuously illuminate a ground patch that is visible to all the antenna elements of the ULA. Thus, the signal (4.9) corresponds to a signal collected in spotlight mode, where the receive antenna pattern is continuously illuminating the center of the ground spot. Using this formulation, the image reconstruction for a single spotlighted patch can be formulated as

$$\hat{g}(\boldsymbol{r}) = \int_{-\infty}^{\infty} ss(r_{rx,0}(\boldsymbol{r};t),t) e^{i2k_c r_{rx,0}(\boldsymbol{r};t)} dt, \tag{4.10}$$

where $r_{rx,0}(\boldsymbol{r};t) = ||\boldsymbol{r}_{rx,0}(t) - \boldsymbol{r}||$ is the monostatic distance between the first antenna element and scene position $\boldsymbol{r}$.

Both (4.8) and (4.10) allow a straightforward implementation of the FFBP algorithm [90]. When using the digital spotlight technique (4.9)–(4.10) for image reconstruction, care needs to be taken in dividing the scene into sub-patches of suitable size. The division is governed by simple geometric considerations. The maximum length of a single spotlighted patch in the along-track-direction is determined by the half-power beamwidth of the receive antenna pattern. Correspondingly, the elevation beamwidth and the length of the synthetic aperture determine the maximum size of the sub-patch in the range direction. The more sub-patches, the more accurate the image reconstruction. For computational efficiency, the size of the sub-patch should be chosen close to the maximum allowable values. However, this comes at a cost of reduced accuracy and image quality at the edges of the spotlight antenna pattern.

In FFBP, the range between the radar and the pixel at $\boldsymbol{r}$ is evaluated using the law of cosines as [89, 90]

$$r_{rx,0}(\boldsymbol{r};y_n) = \sqrt{\rho^2 + y_n^2 - 2\rho y_n \cos\gamma}, \tag{4.11}$$

where (ρ, γ) are the local polar coordinates of $\boldsymbol{r}$. This expression is used in the first stage of the reconstruction algorithm when the first sub-aperture images are reconstructed. Because the length of the sub-aperture in the first stage will always be short (and also the size of a single sub-patch is chosen to be small), the range calculation can be simplified from (4.11). The simplification is achieved by expanding the range term in a Maclaurin series. The same approach has been demonstrated to yield computational savings in the back-projection algorithm [143, 144]. We used the same approximation with our FFBP algorithms in III to increase the computational efficiency of the image reconstruction. Since the sub-apertures in the first stage of the FFBP algorithm are short, (4.11) is approximately linear over the sub-aperture. The first order Maclaurin series expansion of (4.11) is

$$r_{rx,0}(\boldsymbol{r};y_n) \approx \rho - y_n \cos\gamma. \tag{4.12}$$

The validity of this approximation depends on the length of the sub-aperture and on the magnitude of ρ, and has to be evaluated carefully when the length of the sub-aperture or

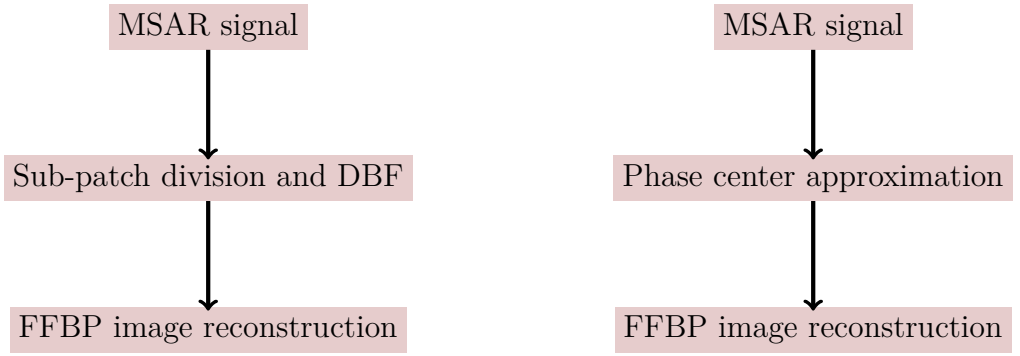

Figure 4.5: The proposed fast time-domain reconstruction processing chains using DBF on receive (left) and the phase center approximation (right).

the size of the image sub-patch increases. The second order term

$$E(y_n) \approx \frac{y_n^2}{2\rho}\left(1 - \cos^2\gamma\right) \tag{4.13}$$

can be used to evaluate the approximation error. We should have $2E \ll \lambda_c$ when utilizing (4.12).

The proposed fast time domain algorithms of III are visualized as flowcharts in Fig. 4.5. The digital spotlighting technique using (4.9)–(4.10) is illustrated on the left hand side of Fig. 4.5. Correspondingly, the technique using the phase center approximation and (4.8) is depicted on the right hand side of Fig. 4.5.

Simulation results

III presented a comparative study between MSAR image reconstruction algorithms. The computational cost and the achieved image quality of the proposed FFBP algorithms were compared to the exact time domain multichannel back-projection algorithm and fast frequency domain algorithms. The data was simulated according to (2.28) with a point target model for g and a range resolution of 0.15 m. A detailed description of the simulation is given in the experimental section of III. The performed tests represented an ideal case for the frequency domain algorithms, producing a good starting point for comparing the algorithm performance.

The interpolations in the RMA and the RDA were performed by oversampling the signal with FFTs and zero padding followed by a cubic spline interpolation. For the back-projection algorithms that require interpolation, we upsampled the original signal that is sampled at the Nyquist rate by a factor of ten by using the FFT algorithm and zero padding in the frequency domain and then used a cubic spline interpolation to obtain the interpolated value. The performance of the fast algorithms (both in terms of speed and image quality) is heavily dependent on the interpolation accuracy [145]. For this reason, we consider the case where the interpolation is performed very accurately with only minor effects on image quality.

The image quality was assessed using well-established image quality metrics from the SAR literature [7, 8]. They included the contrast, maximum residual, cross-range resolution,

Table 4.2: Simulation results of the comparative MSAR study. The results are reproduced from III.

Algorithm	Rel. speed	Contrast	Max. residual [dB]	PSLR [dB]	ISLR [dB]	δy [m]
BP	1	499.2	$-\infty$	-13.37	-11.20	0.0930
FFBP 1	368	402.1	-15	-13.32	-10.57	0.0973
FFBP 2	96	443.0	-17	-13.83	-10.33	0.0947
RSA	5	452.8	-18	-13.47	-10.16	0.0940
RMA	1520	398.8	-14	-13.09	-10.27	0.0946
CSA	12732	272.5	-10	-9.44	-6.11	0.1124

Peak to Side-Lobe Ratio (PSLR), and Integrated Side-Lobe Ratio (ISLR). These quantities were evaluated according to the principles described in [7] and [8]. The algorithms included in the comparative study were Back-Projection (BP) as the benchmark, FFBP algorithms using the digital spotlighting technique (4.10) (FFBP 1) and the phase center approximation (4.8) (FFBP 2), RSA, RMA, and CSA. The results in terms of image quality metrics and computational speed for one of the performed simulation runs are shown in Table 4.2.

As seen from the results in Table 4.2, the FFBP algorithms were approximately two orders of magnitude faster than multichannel BP. FFBP 1 was approximately four times faster than FFBP 2, owing to the significant reduction in the number of slow-time samples in the image reconstruction due to the phase-shift beamforming operation (4.9). However, due to the approximations inherent in the phase-shift beamforming, the image contrast and cross-range resolution were worse than for FFBP 2. RSA, which is based on exact frequency domain matched filtering, produced a better image quality than the FFBP algorithms. However, it was an order of magnitude slower than either of the FFBP algorithms. RMA, which was an order of magnitude faster than any time domain algorithm, resulted in a lower contrast and lower cross-range resolution than RSA or the FFBP algorithms. The approximations of the CSA broke down in this very-high-resolution example, leading to the worst image quality metric values. Fig. 4.6 shows the intensity of one of the PTRs in the reconstructed images of the simulation, which were used to evaluate the image quality. The decreased image quality of CSA is evident from the PTR of Fig. 4.6b. Compared to the PTR of FFBP 1 in Fig. 4.6a, the PTR is more smeared in cross-range and the sidelobe levels are significantly higher.

4.3 Discussion

ISAR

Time domain back-projection has not been extensively used in non-cooperative ISAR image reconstruction mainly due to the high computational burden associated with the data-driven motion compensation. The computational burden of the time domain focusing algorithm of Section 4.1 is higher than for the optimization-based ISAR processing of Chapter 3. Nevertheless, it holds promise by offering a non-approximated way of ISAR image reconstruction in situations where a very high-resolution image is the desired outcome despite complicated target motions. Moreover, it becomes a necessity when the approximations of the more conventional ISAR methods start to break down (e.g. in near-field scenarios). Based on the experimental results, the time domain approach

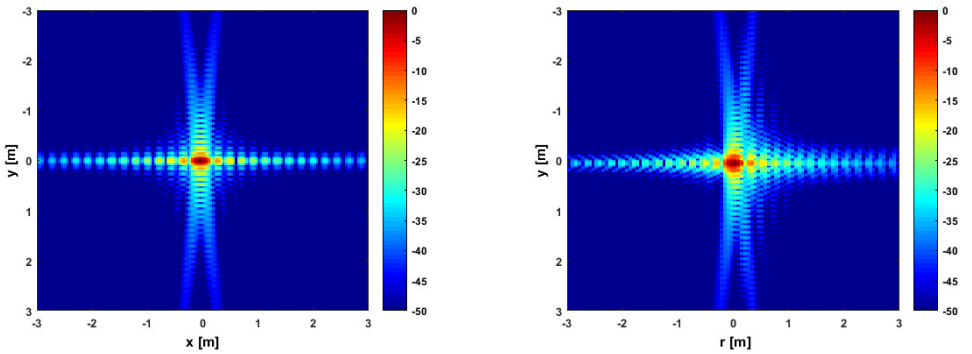

(a) FFBP 1. **(b)** CSA.

Figure 4.6: Comparison of PTRs for FFBP 1 (a) and CSA (b) reveals the decreased image contrast and reduced cross-range resolution of CSA.

outperforms the more conventional approach especially in cases where the rotational motion is highly non-linear.

The computational speed of the contrast optimization algorithm depends on the accuracy of the initial guesses. The range alignment algorithm of Chapter 3 produces a very accurate initial guess and thus a fast convergence for the translation. However, the accuracy of the cross-range scaling algorithm of Chapter 3 (and thus the accuracy of the initial guess for the rotation) suffers from the non-linearity of the rotational motion. To improve the rate of convergence for the rotational part of the optimization the accuracy of the initial guess needs to be further improved. Furthermore, a sensitivity analysis concerning the accuracy of the initial guesses is an important next step of research.

As discussed in the context of the optimization-based ISAR techniques of Chapter 3, the motion compensation procedure can benefit from a priori information obtained from target tracking and expected target kinematics. A possible way to improve the initial guess for the aspect angle would be to use a multichannel ISAR system capable of angular tracking of the target. Combining the range and angular tracks and by assuming a simple kinematic model would produce an initial estimate for both translation and rotation. The accuracy of this estimate would depend on the range resolution and beamwidth (and the Signal to Noise Ratio (SNR)) of the system.

The computational burden of the optimization depends heavily on the image reconstruction, because the ISAR image needs to be reconstructed using the back-projection integral (2.27) several times in the line search procedure of the first order numerical optimization algorithm. To increase the computational efficiency of the proposed approach, the principles of the FFBP algorithm could be used in the image reconstruction. However, this is not straightforward and requires more work due to the complicated non-linear motions of the object, which make the direct application of the FFBP geometry infeasible.

MSAR

Using a SAR system with multiple receive channels all of which are down-converted, digitized, and stored includes a number of benefits. They include for example the reduced requirements for the size of a single antenna element and the PRF, enhanced SNR and

moving target indication capabilities, and an added overall flexibility. Deviations from the ideal operating conditions that are assumed by the frequency domain algorithms complicate the processing and can severely degrade the image quality. The proposed MSAR time domain algorithms provide a better way to accommodate the various non-idealities arising for example from non-ideal flight trajectories and PRF and platform speed variations, without significantly increasing the computational burden or reducing the image quality. The increased range of applicable operating conditions of the fast time domain algorithms mean that they can equally well be used for long-range space-borne HRWS SAR imaging and short-range near-field imaging.

In the FFT-based frequency domain algorithms, the amount of available memory becomes a bottleneck for large image sizes. In the FFBP algorithms, the image reconstruction is carried out in a piecewise manner, allowing a compromise between the required memory and computational speed to be made. The computational speed of the FFBP algorithms can be significantly increased by using a less accurate interpolator than in the simulated example of Section 4.2. However, this comes at the cost of degraded image quality. Thus, the FFBP image reconstruction offers a way to make trade-offs between image quality and computational speed that the conventional frequency domain algorithms lack.

Validation of the proposed methods by an experimental short-range MSAR system remains as future work. In addition, more work needs to be done to develop computationally efficient FFBP implementations for cases where the phase center approximation and phase-shift beamforming are no longer applicable. This will further extend the area of applicability of MSAR imaging into a wider range of allowable operating conditions. Another step of future research is the application of more advanced MSAR imaging modalities such as ATI and STAP. These applications also benefit from fast and accurate image reconstruction algorithms.

5 Conclusion

Chapters 3 and 4 have demonstrated the increased imaging performance of the proposed algorithms for both non-cooperative ISAR and MSAR. Importantly, the optimization-based ISAR processing signal processing chain presented in Chapter 3 was shown to surpass the conventional methods with a lower computational cost. The time domain image reconstruction algorithms of Chapter 4 further increased the ISAR imaging performance, albeit at the cost of increased computational complexity.

The optimization-based ISAR processing proposed in Chapter 3 uses mathematical optimization in every part of data-driven motion compensation and ISAR image reconstruction. Both the computational speed and estimation accuracy of range alignment were improved by combining previously suggested loss functions and utilizing first and second order numerical optimization. The time window optimization process was enhanced by improving the motion compensation process included in the loss evaluation. Theoretical results were derived for COA and cross-range scaling, which simplify the implementation aspects of the algorithms as well as reduce their computational burden. The ISAR image reconstruction based on TFRs was improved by choosing the kernel function of the TFR by maximizing the image contrast. Together, these contributions yielded increased imaging performance in terms of the image contrast and spatial resolution under complicated target motion dynamics.

A time domain focusing algorithm for ISAR image reconstruction using the principles of contrast optimization was proposed. It was shown to increase the imaging performance in test scenarios including highly non-linear rotational motion during the CPI. By utilizing carefully selected initial guesses for both the translation and rotation, the algorithm optimizes the image contrast by using first order local numerical optimization. The increased imaging performance comes at a cost of increasing the computation time from a matter of seconds to a few minutes. Based on the experimental evidence, the time domain focusing algorithm is able to extend the envelope of situations where non-cooperative ISAR imaging is applicable. Fast time domain algorithms based on DBF, the phase center approximation, and the FFBP algorithm were proposed for MSAR imaging. In numerical simulations, they were shown to provide a good compromise between computational efficiency and image quality.

The numerical validation of the algorithms was done in a controlled environment using simulated and turntable-based radar data. While this provides a good starting point, an essential next step is to test the algorithms with real non-cooperative ISAR and MSAR data. Moreover, an extension to three-dimensional imaging geometries as well as moving radar platforms remains as future work. The time domain formulations presented in this thesis provide a solid foundation for handling these more complex scenarios.

Significantly, the proposed algorithms improve the radar imaging performance under challenging operating conditions including non-standard imaging geometries and complex relative motions. This not only produces images with better quality in existing radar imaging applications, but also can increase the number of potential application areas of radar imaging. The increased applicability benefits conventional older radar systems as well as the more recent industrial applications utilizing low-cost short-range SDRSs. The proposed algorithms not only improve SAR imaging but may also be applicable in other applications such as computer-aided tomography widely used in the medical field. In a broader context, this work continues the trend started in the 1980s of applying sophisticated signal and image processing techniques for radar applications.

Bibliography

[1] R. K. Raney, "A new and fundamental Fourier transform pair," in *Proceedings of IEEE International Geoscience and Remote Sensing Symposium (IGARSS)*, Houston, TX, USA, May 1992, pp. 106–107.

[2] M. I. Skolnik, *Introduction to radar systems.* McGraw-Hill, 2001.

[3] A. W. Rihaczek, *Principles of High-Resolution Radar.* Norwood, MA, USA: Artech House, 1996.

[4] D. R. Wehner, *High resolution radar.* Norwood, MA, USA: Artech House, Inc., 1987.

[5] S. M. Patole, M. Torlak, D. Wang, and M. Ali, "Automotive radars: A review of signal processing techniques," *IEEE Signal Processing Magazine*, vol. 34, no. 2, pp. 22–35, Mar. 2017.

[6] W. Wiesbeck, "SDRS: Software-defined radar sensors," in *Proceedings of IEEE International Geoscience and Remote Sensing Symposium (IGARSS)*, Sydney, Australia, Jul. 2001, pp. 187–191.

[7] J. C. Curlander and R. N. McDonough, *Synthetic Aperture Radar: Systems and Signal Processing.* New York: Wiley, 1991.

[8] W. G. Carrara, R. S. Goodman, and R. M. Majewski, *Spotlight Synthetic Aperture Radar: Signal Processing Algorithms.* Boston, MA: Artech House, 1995.

[9] M. Soumekh, *Synthetic Aperture Radar Signal Processing with MATLAB Algorithms.* New York: Wiley, 1999.

[10] A. Moreira, P. Prats-Iraola, M. Younis, G. Krieger, I. Hajnsek, and K. P. Papathanassiou, "A tutorial on synthetic aperture radar," *IEEE Geoscience and Remote Sensing Magazine*, vol. 1, no. 1, pp. 6–43, Mar. 2013.

[11] A. Reigber, R. Scheiber, M. Jager, P. Prats-Iraola, I. Hajnsek, T. Jagdhuber, K. P. Papathanassiou, M. Nannini, E. Aguilera, S. Baumgartner, R. Horn, A. Nottensteiner, and A. Moreira, "Very-high-resolution airborne synthetic aperture radar imaging: Signal processing and applications," *Proceedings of the IEEE*, vol. 101, no. 3, pp. 759–783, Mar. 2013.

[12] V. C. Chen and M. Martorella, *Inverse synthetic aperture radar.* SciTech Publishing, 2014.

[13] F. Berizzi and G. Corsini, "Autofocusing of inverse synthetic aperture radar images using contrast optimization," *IEEE Transactions on Aerospace and Electronic Systems*, vol. 32, no. 3, pp. 1185–1191, Jul. 1996.

[14] L. Xi, L. Guosui, and J. Ni, "Autofocusing of ISAR images based on entropy minimization," *IEEE Transactions on Aerospace and Electronic Systems*, vol. 35, no. 4, pp. 1240–1252, Oct. 1999.

[15] J. Wang and D. Kasilingam, "Global range alignment for ISAR," *IEEE Transactions on Aerospace and Electronic Systems*, vol. 39, no. 1, pp. 351–357, Jan. 2003.

[16] J. Wang and X. Liu, "Improved global range alignment for ISAR," *IEEE Transactions on Aerospace and Electronic Systems*, vol. 43, no. 3, pp. 1070–1075, Jul. 2007.

[17] R. L. Morrison, M. N. Do, and D. C. Munson, "SAR image autofocus by sharpness optimization: a theoretical study," *IEEE Transactions on Image Processing*, vol. 16, no. 9, pp. 2309–2321, Sep. 2007.

[18] H. Wu, D. Grenier, G. Y. Delisle, and D.-G. Fang, "Translational motion compensation in ISAR image processing," *IEEE Transactions on Image Processing*, vol. 4, no. 11, pp. 1561–1571, Nov. 1995.

[19] D. Zhu, L. Wang, Y. Yu, Q. Tao, and Z. Zhu, "Robust ISAR range alignment via minimizing the entropy of the average range profile," *IEEE Geoscience and Remote Sensing Letters*, vol. 6, no. 2, pp. 204–208, Apr. 2009.

[20] F. Berizzi, G. Corsini, M. Diani, and M. Veltroni, "Autofocus of wide azimuth angle SAR images by contrast optimization," in *Proceedings of IEEE International Geoscience and Remote Sensing Symposium (IGARSS)*, Lincoln, NE, USA, May 1996, pp. 1230–1232.

[21] P. T. Gough and R. G. Lane, "Autofocussing SAR and SAS images using a conjugate gradient search algorithm," in *Proceedings of IEEE International Geoscience and Remote Sensing Symposium (IGARSS)*, Seattle, WA, USA, Jul. 1998, pp. 621–623.

[22] J. R. Fienup, "Synthetic aperture radar autofocus by maximizing sharpness," *Optics Letters*, vol. 25, no. 4, pp. 221–223, Feb. 2000.

[23] ———, "Detecting moving targets in SAR imagery by focusing," *IEEE Transactions on Aerospace and Electronic Systems*, vol. 37, no. 3, pp. 794–809, Jul. 2001.

[24] S. A. Fortune, M. P. Hayes, and P. T. Gough, "Statistical autofocus of synthetic aperture sonar images using contrast optimization," in *Proceedings of IEEE International Geoscience and Remote Sensing Symposium (IGARSS)*, Sydney, Australia, Jul. 2001, pp. 1509–1511.

[25] J. R. Fienup and J. J. Miller, "Aberration correction by maximizing generalized sharpness metrics," *Journal of the Optical Society of America A*, vol. 20, no. 4, pp. 609–620, Apr. 2003.

[26] F. Berizzi, M. Martorella, B. Haywood, E. D. Mese, and S. Bruscoli, "A survey on ISAR autofocusing techniques," in *Proceeding of the International Conference on Image Processing (ICIP)*, Oct. 2004, pp. 9–12.

[27] M. Martorella, F. Berizzi, and B. Haywood, "Contrast maximization based technique for 2-D ISAR autofocusing," *IEE Proceedings on Radar, Sonar and Navigation*, vol. 152, no. 4, pp. 253–262, Aug. 2005.

[28] T. J. Schulz, "Optimal sharpness function for SAR autofocus," *IEEE Signal Processing Letters*, vol. 14, no. 1, pp. 27–30, Jan. 2007.

[29] F. Berizzi, M. Martorella, A. Cacciamano, and A. Capria, "A contrast-based algorithm for synthetic range-profile motion compensation," *IEEE Transactions on Geoscience and Remote Sensing*, vol. 46, no. 10, pp. 3053–3062, Oct. 2008.

[30] P. H. Eichel, D. C. Ghiglia, and C. V. Jakowatz, "Speckle processing method for synthetic-aperture-radar phase correction," *Optics Letters*, vol. 14, no. 1, pp. 1–3, Jan. 1989.

[31] C. V. Jakowatz and D. E. Wahl, "Eigenvector method for maximum-likelihood estimation of phase errors in synthetic-aperture radar imagery," *Optics Letters*, vol. 10, no. 12, pp. 2539–2546, Dec. 1993.

[32] D. E. Wahl, P. H. Eichel, D. C. Ghiglia, and C. V. Jakowatz, "Phase gradient autofocus - a robust tool for high resolution SAR phase correction," *IEEE Transactions on Aerospace and Electronic Systems*, vol. 30, no. 3, pp. 827–835, Jul. 1994.

[33] D. E. Wahl, C. V. Jakowatz, and P. A. Thompson, "New approach to strip-map sar autofocus," in *Sixth IEEE Digital Signal Processing Workshop*, Yosemite National Park, CA, USA, Oct. 1994, pp. 53–56.

[34] H. L. Chan and T. S. Yeo, "Noniterative quality phase gradient autofocus (QPGA) algorithm for spotlight SAR imagery," *IEEE Transactions on Geoscience and Remote Sensing*, vol. 36, no. 5, pp. 1531–1539, Sep. 1998.

[35] W. Ye, T. S. Yeo, and Z. Bao, "Weighted least-squares estimation of phase errors for SAR/ISAR autofocus," *IEEE Transactions on Geoscience and Remote Sensing*, vol. 37, no. 5, pp. 2487–2494, Sep. 1999.

[36] D. G. Thompson, J. S. Bates, D. V. Arnold, and D. G. Long, "Extending the phase gradient autofocus algorithm for low-altitude stripmap mode SAR," in *Proceedings of IEEE International Geoscience and Remote Sensing Symposium (IGARSS)*, Hamburg, Germany, Jul. 1999, pp. 564–566.

[37] H. J. Callow, M. P. Hayes, and P. T. Gough, "Autofocus of multi-band, shallow-water, synthetic aperture sonar imagery using shear averaging," in *Proceedings of IEEE International Geoscience and Remote Sensing Symposium (IGARSS)*, Sydney, Australia, Jul. 2001, pp. 1601–1603.

[38] P. Tsakalides and C. L. Nikias, "High-resolution autofocus techniques for SAR imaging based on fractional lower-order statistics," *IEE Proceedings on Radar, Sonar and Navigation*, vol. 148, no. 5, pp. 267–276, Oct. 2001.

[39] H. J. Callow, M. P. Hayes, and P. T. Gough, "Stripmap phase gradient autofocus," in *OCEANS 2003. Proceedings*, vol. 5, San Diego, CA, USA, Sep. 2003, pp. 2414–2421.

[40] W. L. van Rossum, M. P. G. Otten, and R. J. P. V. Bree, "Extended PGA for range migration algorithms," *IEEE Transactions on Aerospace and Electronic Systems*, vol. 42, no. 2, pp. 478–488, Apr. 2006.

[41] K. A. C. de Macedo, R. Scheiber, and A. Moreira, "An autofocus approach for residual motion errors with application to airborne repeat-pass SAR interferometry," *IEEE Transactions on Geoscience and Remote Sensing*, vol. 46, no. 10, pp. 3151–3162, Oct. 2008.

[42] D. Zhu, R. Jiang, X. Mao, and Z. Zhu, "Multi-subaperture PGA for SAR autofocusing," *IEEE Transactions on Aerospace and Electronic Systems*, vol. 49, no. 1, pp. 468–488, Jan. 2013.

[43] M. Martorella and F. Berizzi, "Time windowing for highly focused ISAR image reconstruction," *IEEE Transactions on Aerospace and Electronic Systems*, vol. 41, no. 3, pp. 992–1007, Jul. 2005.

[44] R. P. Perry, R. C. DiPietro, and R. L. Fante, "SAR imaging of moving targets," *IEEE Transactions on Aerospace and Electronic Systems*, vol. 35, no. 1, pp. 188–200, Jan. 1999.

[45] M. Xing, R. Wu, J. Lan, and Z. Bao, "Migration through resolution cell compensation in ISAR imaging," *IEEE Geoscience and Remote Sensing Letters*, vol. 1, no. 2, pp. 141–144, Apr. 2004.

[46] M. Xing, R. Wu, and Z. Bao, "High resolution ISAR imaging of high speed moving targets," *IEE Proceedings on Radar, Sonar and Navigation*, vol. 152, no. 2, pp. 58–67, Apr. 2005.

[47] D. Kirkland, "Imaging moving targets using the second-order keystone transform," *IET Radar, Sonar and Navigation*, vol. 5, no. 8, pp. 902–910, Oct. 2011.

[48] V. C. Chen, "Reconstruction of inverse synthetic aperture radar image using adaptive time-frequency wavelet transform," in *SPIE's 1995 Symposium on OE/Aerospace Sensing and Dual Use Photonics*. International Society for Optics and Photonics, 1995, pp. 373–386.

[49] L. C. Trintinalia and H. Ling, "Joint time-frequency ISAR using adaptive processing," *IEEE Transactions on Antennas and Propagation*, vol. 45, no. 2, pp. 221–227, Feb. 1997.

[50] V. C. Chen and S. Qian, "Joint time-frequency transform for radar range-doppler imaging," *IEEE Transactions on Aerospace and Electronic Systems*, vol. 34, no. 2, pp. 486–499, Apr. 1998.

[51] Y. Wang, H. Ling, and V. C. Chen, "ISAR motion compensation via adaptive joint time-frequency technique," *IEEE Transactions on Aerospace and Electronic Systems*, vol. 34, no. 2, pp. 670–677, Apr. 1998.

[52] X. Xia, G. Wang, and V. C. Chen, "Quantitative SNR analysis for ISAR imaging using joint time-frequency analysis - short time fourier transform," *IEEE Transactions on Aerospace and Electronic Systems*, vol. 38, no. 2, pp. 649–659, Apr. 2002.

[53] T. Thayaparan, G. Lampropoulos, S. K. Wong, and E. Riseborough, "Application of adaptive joint time-frequency algorithm for focusing distorted ISAR images from simulated and measured radar data," *IEE Proceedings on Radar, Sonar and Navigation*, vol. 150, no. 4, pp. 213–220, Aug. 2003.

[54] F. Berizzi, E. D. Mese, M. Diani, and M. Martorella, "High-resolution ISAR imaging of maneuvering targets by means of the range instantaneous doppler technique: modeling and performance analysis," *IEEE Transactions on Image Processing*, vol. 10, no. 12, pp. 1880 – 1890, Dec. 2001.

[55] V. C. Chen and H. Ling, *Time-frequency transforms for radar imaging and signal analysis*. Artech House, 2002.

[56] I. Djurović, T. Thayaparan, and L. Stanković, "Adaptive local polynomial fourier transform in ISAR," *EURASIP Journal on Applied Signal Processing*, vol. 2006, pp. 129 – 129, 2006.

[57] L. J. Stankovic, T. Thayaparan, M. Dakovic, and V. Popovic, "S-method in radar imaging," in *Proceedings of the14th European Signal Processing Conference*, Florence, Italy, Sep. 2006, pp. 1 – 5.

[58] L. J. Stankovic, T. Thayaparan, V. Popovic, I. Djurovic, and M. Dakovic, "Adaptive S-method for SAR/ISAR imaging," *EURASIP Journal on Advances in Signal Processing*, vol. 2008, pp. 1 – 10, 2008.

[59] T. Thayaparan, L. Stankovic, C. Wernik, and M. Dakovic, "Real-time motion compensation, image formation and image enhancement of moving targets in ISAR and SAR using s-method-based approach," *IET Signal Processing*, vol. 2, no. 3, pp. 247 – 264, 2008.

[60] L. Stanković, M. Daković, and T. Thayaparan, *Time-frequency signal analysis with applications*. Artech House, 2014.

[61] S. Werness, W. Carrara, L. Joyce, and D. Franczak, "Moving target imaging algorithm for SAR data," *IEEE Transactions on Aerospace and Electronic Systems*, vol. 26, no. 1, pp. 57 – 67, Jan. 1990.

[62] Q. Zhang, T. S. Yeo, G. Du, and S. Zhang, "Estimation of three-dimensional motion parameters in interferometric ISAR imaging," *IEEE Transactions on Geoscience and Remote Sensing*, vol. 42, no. 2, pp. 292 – 300, Feb. 2004.

[63] F. Zhou, R. Wu, M. Xing, and Z. Bao, "Approach for single channel SAR ground moving target imaging and motion parameter estimation," *IET Radar, Sonar and Navigation*, vol. 1, no. 1, pp. 59 – 66, Feb. 2007.

[64] M. Martorella, "Novel approach for ISAR image cross-range scaling," *IEEE Transactions on Aerospace and Electronic Systems*, vol. 44, no. 1, pp. 281 – 294, Jan. 2008.

[65] M. Martorella, E. Giusti, F. Berizzi, A. Bacci, and E. D. Mese, "ISAR based techniques for refocusing non-cooperative targets in SAR images," *IET Radar, Sonar and Navigation*, vol. 6, no. 5, pp. 332 – 340, Jun. 2012.

[66] F. Prodi, "ISAR cross-range scaling using a correlation based functional," in *IEEE RADAR 2008*, Rome, Italy, May 2008, pp. 1 – 6.

[67] C.-M. Yeh, J.Yang, Y.-N. Peng, and X.-M. Shan, "Rotation estimation for ISAR targets with a space-time analysis technique," *IEEE Geoscience and Remote Sensing Letters*, vol. 8, no. 5, pp. 899 – 903, Sep. 2011.

[68] C.-M. Yeh, J. Xu, Y.-N. Peng, and X.-T. Wang, "Cross-range scaling for ISAR based on image rotation correlation," *IEEE Geoscience and Remote Sensing Letters*, vol. 6, no. 3, pp. 597 – 601, Jul. 2009.

[69] S.-H. Park, H.-T. Kim, and K.-T. Kim, "Cross-range scaling algorithm for ISAR images using 2-D Fourier transform and polar mapping," *IEEE Transactions on Geoscience and Remote Sensing*, vol. 49, no. 2, pp. 868 – 877, Feb. 2011.

[70] S. Brisken, M. Martorella, T. Mathy, C. Wasserzier, J. G. Worms, and J. H. G. Ender, "Motion estimation and imaging with a multistatic ISAR system," *IEEE Transactions on Aerospace and Electronic Systems*, vol. 50, no. 3, pp. 1701 – 1714, Jul. 2014.

[71] S. Brisken and M. Martorella, "Multistatic ISAR autofocus with an image entropy-based technique," *IEEE Aerospace and Electronic Systems Magazine*, vol. 29, no. 7, pp. 30 – 36, Jul. 2014.

[72] J. Jylhä, M. Väilä, H. Perälä, V. Väisänen, R. Vehmas, J. Kylmälä, V.-J. Salminen, and A. Visa, "On SAR processing using pixel-wise matched kernels," in *Proceedings of the 11th European Radar Conference (EuRAD 2014)*, Rome, Italy, Oct. 2014, pp. 97 – 100.

[73] M. Xing, X. Jiang, R. Wu, F. Zhou, and Z. Bao, "Motion compensation for UAV SAR based on raw radar data," *IEEE Transactions on Geoscience and Remote Sensing*, vol. 47, no. 8, pp. 2870 – 2883, Aug. 2009.

[74] L. Zhang, Z. Qiao, M. Xing, L. Yang, and Z. Bao, "A robust motion compensation approach for UAV SAR imagery," *IEEE Transactions on Geoscience and Remote Sensing*, vol. 50, no. 8, pp. 3202 – 3218, Aug. 2012.

[75] D. C. Munson, J. D. O'Brien, and W. K. Jenkins, "A tomographic formulation of spotlight-mode synthetic aperture radar," *Proceedings of the IEEE*, vol. 72, no. 8, pp. 917 – 925, Aug. 1983.

[76] C. V. Jakowatz and D. E. Wahl, "Considerations for autofocus of spotlight-mode SAR imagery created using a beamforming algorithm," in *Proc. SPIE - Algorithms Synthetic Aperture Radar Imagery*, vol. 7337, 2009, pp. 73 370A – 1 – 73 370A – 9.

[77] A. Moreira and H. Yonghong, "Airborne SAR processing of highly squinted data using a chirp scaling approach with integrated motion compensation," *IEEE Transactions on Geoscience and Remote Sensing*, vol. 32, no. 5, pp. 1029 – 1040, Sep. 1994.

[78] A. Moreira, J. Mittermayer, and R. Scheiber, "Extended chirp scaling algorithm for air- and spaceborne SAR data processing in stripmap and ScanSAR imaging modes," *IEEE Transactions on Geoscience and Remote Sensing*, vol. 34, no. 5, pp. 1123 – 1136, Sep. 1996.

[79] A. Reigber, E. Alivizatos, A. Potsis, and A. Moreira, "Extended wavenumber-domain synthetic aperture radar focusing with integrated motion compensation," *IEE Proceedings on Radar, Sonar and Navigation*, vol. 153, no. 3, pp. 301 – 310, Jun. 2006.

[80] J. N. Ash, "An autofocus method for backprojection imagery in synthetic aperture radar," *IEEE Geoscience and Remote Sensing Letters*, vol. 9, no. 1, pp. 104–108, Jan. 2012.

[81] J. Torgrimsson, P. Dammert, H. Hellsten, and L. M. H. Ulander, "Factorized geometrical autofocus for synthetic aperture radar processing," *IEEE Transactions on Geoscience and Remote Sensing*, vol. 52, no. 10, pp. 6674–6687, Oct. 2014.

[82] ———, "An efficient solution to the factorized geometrical autofocus problem," *IEEE Transactions on Geoscience and Remote Sensing*, vol. 54, no. 8, pp. 4732–4748, Aug. 2016.

[83] R. Bamler, "A comparison of range-Doppler and wavenumber domain SAR focusing algorithms," *IEEE Transactions on Geoscience and Remote Sensing*, vol. 30, no. 4, pp. 706–713, Jul. 1992.

[84] I. Cumming and F. Wong, *Digital Processing of Synthetic Aperture Radar Data: Algorithms and Implementation*. Boston, MA: Artech House, 2005.

[85] R. K. Raney, H. Runge, R. Bamler, I. G. Cumming, and F. H. Wong, "Precision SAR processing using chirp scaling," *IEEE Transactions on Geoscience and Remote Sensing*, vol. 32, no. 4, pp. 786–799, Jul. 1994.

[86] F. Rocca, C. Cafforio, and C. Prati, "Synthetic aperture radar: A new application for wave equation techniques," *Geophysical Prospecting*, vol. 37, no. 7, pp. 809–830, Oct. 1989.

[87] C. Cafforio, C. Prati, and F. Rocca, "SAR data focusing using seismic migration techniques," *IEEE Transactions on Aerospace and Electronic Systems*, vol. 27, no. 2, pp. 194–207, Mar. 1991.

[88] M. D. Desai and W. K. Jenkins, "Convolution backprojection image reconstruction for spotlight mode synthetic aperture radar," *IEEE Transactions on Image Processing*, vol. 1, no. 4, pp. 505–517, Oct. 1992.

[89] A. F. Yegulalp, "Fast backprojection algorithm for synthetic aperture radar," in *Proceedings of the 1999 IEEE Radar Conference*, Waltham, MA, USA, Apr. 1999, pp. 60–65.

[90] L. M. H. Ulander, H. Hellsten, and G. Stenström, "Synthetic-aperture radar processing using fast factorized back-projection," *IEEE Transactions on Aerospace and Electronic Systems*, vol. 39, no. 3, pp. 760–776, Jul. 2003.

[91] M. Rodriguez-Cassola, P. Prats, G. Krieger, and A. Moreira, "Efficient time-domain image formation with precise topography accommodation for general bistatic SAR configurations," *IEEE Transactions on Aerospace and Electronic Systems*, vol. 47, no. 4, pp. 2949–2966, Oct. 2011.

[92] V. T. Vu, T. K. Sjögren, and M. I. Pettersson, "Fast time-domain algorithms for UWB bistatic SAR processing," *IEEE Transactions on Aerospace and Electronic Systems*, vol. 49, no. 3, pp. 1982–1994, Jul. 2013.

[93] O. Ponce, P. Prats, M. Rodriguez-Cassola, R. Scheiber, and A. Reigber, "Processing of circular SAR trajectories with fast factorized back-projection," in *Proceedings of IEEE International Geoscience and Remote Sensing Symposium (IGARSS)*, Vancouver, BC, Canada, Jul. 2011, pp. 3692–3695.

[94] A. Currie and M. Brown, "Wide-swath SAR," *IEE Proceedings F, Radar and Signal Processing*, vol. 139, no. 2, pp. 122–135, Apr. 1992.

[95] M. Younis, C. Fischer, and W. Wiesbeck, "Digital beamforming in SAR systems," *IEEE Transactions on Geoscience and Remote Sensing*, vol. 41, no. 71, pp. 1735–1739, Jul. 2003.

[96] N. Gebert, G. Krieger, and A. Moreira, "Digital beamforming on receive: Techniques and optimization strategies for high resolution wide-swath SAR imaging," *IEEE Transactions on Aerospace and Electronic Systems*, vol. 45, no. 2, pp. 564–592, Apr. 2009.

[97] A. Jain, "Multibeam synthetic aperture radar for global oceanography," *IEEE Transactions on Antennas and Propagation*, vol. AP-27, no. 4, pp. 535–538, Jul. 1979.

[98] B. R. Jean and J. W. Rouse, "A multiple beam synthetic aperture radar design concept for geoscience applications," *IEEE Transactions on Geoscience and Remote Sensing*, vol. GRS-21, no. 2, pp. 201–207, Apr. 1983.

[99] N. A. Goodman, S. C. Lin, D. Rajakrishna, and J. M. Stiles, "Processing of multiple-receiver spaceborne arrays for wide-area SAR," *IEEE Transactions on Geoscience and Remote Sensing*, vol. 40, no. 4, pp. 841–852, Apr. 2002.

[100] G. Krieger and A. Moreira, "Multidimensional waveform encoding: A new digital beamforming technique for synthetic aperture radar remote sensing," *IEEE Transactions on Geoscience and Remote Sensing*, vol. 46, no. 1, pp. 31–46, Jan. 2008.

[101] ———, "Potential of digital beamforming in bi- and multistatic SAR," in *Proceedings of IEEE International Geoscience and Remote Sensing Symposium (IGARSS)*, Touluse, France, Jul. 2003, pp. 527–529.

[102] G. Krieger, M. Younis, N. Gebert, S. Huber, F. Bordoni, A. Patuychenko, and A. Moreira, "Advanced digital beamforming concepts for future SAR systems," in *Proceedings of IEEE International Geoscience and Remote Sensing Symposium (IGARSS)*, Jul. 2003, pp. 245–248.

[103] S. Huber, M. Younis, A. Patyuchenko, G. Krieger, and A. Moreira, "Spaceborne reflector SAR systems with digital beamforming," *IEEE Transactions on Aerospace and Electronic Systems*, vol. 48, no. 4, pp. 3473–3493, Oct. 2012.

[104] L. J. Cutrona, "Comparison of sonar system performance achievable using synthetic-aperture techniques with the performance achievable by more conventional means," *The Journal of the Acoustical Society of America*, vol. 58, no. 2, pp. 336–348, Aug. 1975.

[105] M. P. Hayes and P. T. Gough, "Synthetic aperture sonar: a review of current status," *IEEE Journal of Oceanic Engineering*, vol. 34, no. 3, pp. 207–224, Jul. 2009.

[106] H. J. Callow, "Signal processing for synthetic aperture sonar image enhancement," Ph.D. dissertation, University of Canterbury, Christchurch, New Zealand, 2003.

[107] A. Belletini and M. A. Pinto, "Theoretical accuracy of synthetic aperture sonar micronavigation using a displaced phase-center antenna," *IEEE Journal of Oceanic Engineering*, vol. 27, no. 4, pp. 780 – 789, Oct. 2002.

[108] B. L. Douglas, H. Lee, and C. D. Loggins, "A multiple-receiver synthetic-aperture active sonar imaging system," in *OCEANS'92. Mastering the Oceans Through Technology. Proceedings.*, vol. 1. IEEE, 1992, pp. 300 – 305.

[109] B. L. Douglas and H. Lee, "Synthetic-aperture sonar imaging with a multiple-element receiver array," in *Acoustics, Speech, and Signal Processing, 1993. ICASSP-93., 1993 IEEE International Conference on*, vol. 5, 1993, pp. 445 – 448.

[110] M. A. Lawlor, A. E. Adams, O. R. Hinton, V. S. Riyait, and B. Sharif, "Methods for increasing the azimuth resolution and mapping rate of a synthetic aperture sonar," in *OCEANS'94.'Oceans Engineering for Today's Technology and Tomorrow's Preservation.'Proceedings*, vol. 3. IEEE, 1994, pp. 565 – 570.

[111] P. T. Gough, M. P. Hayes, and D. R. Wilkinson, "An efficient image reconstruction algorithm for a multiple hydrophone array synthetic aperture sonar," in *Proceedings of the fifth European Conference on Underwater Acoustics (ECUA)*, 2000, pp. 395 – 400.

[112] G. Krieger, N. Gebert, and A. Moreira, "Unambiguous SAR signal reconstruction from nonuniform displaced phase center sampling," *IEEE Geoscience and Remote Sensing Letters*, vol. 1, no. 4, pp. 260 – 264, Oct. 2004.

[113] N. Gebert, "Multi-channel azimuth processing for high resolution wide-swath SAR imaging," Ph.D. dissertation, University of Karlsruhe, Karlsruhe, Germany, 2009.

[114] D. Cerutti-Maori, I. Sikaneta, J. Klare, and C. H. Gierull, "MIMO SAR processing for multichannel high-resolution wide-swath radars," *IEEE Transactions on Geoscience and Remote Sensing*, vol. 52, no. 8, pp. 5034 – 5055, Aug. 2014.

[115] I. Sikaneta, C. H. Gierull, and D. Cerutti-Maori, "Optimum signal processing for multichannel SAR: with application to high-resolution wide-swath imaging," *IEEE Transactions on Geoscience and Remote Sensing*, vol. 52, no. 10, pp. 6095 – 6109, Oct. 2014.

[116] H. Perälä, M. Väilä, J. Jylhä, J. Kylmälä, V.-J. Salminen, and A. Visa, "On efficient characterization of radar targets with scatterer sets for target recognition using commercial ray tracing software," in *2014 IEEE Radar Conference*, Cincinnati, OH, USA, May 2014, pp. 260 – 264.

[117] M. A. Richards, J. A. Scheer, W. A. Holm, and W. L. Melvin, *Principles of Modern Radar: Basic Principles*. SciTech Publishing, 2010.

[118] C. V. Jakowatz Jr., D. Wahl, P. Eichel, D. Ghiglia, and P. Thompson, *Spotlight-mode Synthetic Aperture Radar: A signal processing approach*. Boston, MA: Kluwer Academic Publishers, 1996.

[119] V. Janse van Rensburg, A. Mishra, and W. Nel, "Quality measures for HRR alignment based ISAR imaging algorithms," in *2013 IEEE Radar Conference*, Ottawa, ON, Canada, May 2013, pp. 1–4.

[120] R. L. Morrison, M. N. Do, and D. C. Munson, "MCA: a multichannel approach to SAR autofocus," *IEEE Transactions on Image Processing*, vol. 18, no. 4, pp. 840–853, Apr. 2009.

[121] K.-H. Liu and D. C. Munson, "Fourier-domain multichannel autofocus for synthetic aperture radar," *IEEE Transactions on Image Processing*, vol. 20, no. 12, pp. 3544–3552, Dec. 2011.

[122] J. L. Walker, "Range-Doppler imaging of rotating objects," *IEEE Transactions on Aerospace and Electronic Systems*, vol. AES-16, no. 1, pp. 23–52, Jan. 1980.

[123] C. H. Casteel, L. Gorham, M. J. Minardi, S. Scarborough, and K. D. Naidu, "A challenge problem for 2D/3D imaging of targets from a volumetric data set in an urban environment," in *Proc. SPIE 6568, E. G. Zelnio and F. D. Garber eds.*, Apr. 2007.

[124] L. Cohen, *Time-frequency analysis: theory and applications*. NJ, USA: Prentice-Hall, 1995.

[125] D. Pastina, A. Montanari, and A. Aprile, "Motion estimation and optimum time selection for ship ISAR imaging," in *Proceedings of the 2003 IEEE Radar Conference*, May 2003, pp. 7–14.

[126] D. Pastina and C. Spina, "Slope-based frame selection and scaling technique for ship ISAR imaging," *IET Signal Processing*, vol. 2, no. 3, pp. 265–276, Sep. 2008.

[127] P. A. Rosen, S. Hensley, R. I. Joughin, F. K. Li, S. N. Madsen, E. Rodriguez, and R. M. Goldstein, "Synthetic aperture radar interferometry," *Proceedings of the IEEE*, vol. 88, no. 3, pp. 333–381, Mar. 2000.

[128] J. R. Guerci, *Space-time adaptive processing for radar*. Artech House, 2014.

[129] M. Younis, "Digital beamforming for high-resolution wide swath real and synthetic aperture radar," Ph.D. dissertation, University of Karlsruhe, Karlsruhe, Germany, 2004.

[130] D. R. Wilkinson, "Efficient image reconstruction techniques for a multiple-receiver synthetic aperture sonar," Master's thesis, University of Canterbury, Christchurch, New Zealand, 2001.

[131] M. Soumekh, "A system model and inversion for synthetic aperture radar imaging," *IEEE Transactions on Image Processing*, vol. 1, no. 1, pp. 64–76, Jan. 1992.

[132] ———, "Range stacking: An interpolation-free SAR reconstruction algorithm," in *Proc. SPIE Conf. Algorithms for Synthetic Aperture Radar Imagery V*, vol. 3370, Sep. 1998, pp. 13–24.

[133] B. D. Steinberg, "Microwave imaging of aircraft," *Proceedings of the IEEE*, vol. 76, no. 12, pp. 1578–1592, Dec. 1988.

[134] S. A. Fortune, "Phase error estimation for synthetic aperture imagery," Ph.D. dissertation, University of Canterbury, Christchurch, New Zealand, 2005.

[135] A. W. Paeth, "A fast algorithm for general raster rotation," in *Graphics interface '86 - Vision interface '86*, May 1986, pp. 77–81.

[136] M. Unser, P. Thevenaz, and L. Yaroslavsky, "Convolution-based interpolation for fast, high-quality rotation of images," *IEEE Transactions on Image Processing*, vol. 4, no. 10, pp. 1371–1381, Oct. 1995.

[137] S. Stankovic, I. Orovic, and A. Krylov, "Two-dimensional hermite S-method for high-resolution inverse synthetic aperture radar imaging applications," *IET Signal Processing*, vol. 4, no. 4, pp. 352–362, Aug. 2010.

[138] L. Stankovic, "A method for time-frequency analysis," *IEEE Transactions on Signal Processing*, vol. 42, no. 1, pp. 225–229, Jan. 1994.

[139] F. Auger and P. Flandrin, "Improving the readability of time-frequency and time-scale representations by the reassignment method," *IEEE Transactions on Signal Processing*, vol. 43, no. 5, pp. 1068–1089, May 1995.

[140] R. Wang and Y. C. Jiang, "ISAR ship imaging based on reassigned smoothed pseudo Wigner-Ville distribution," in *2010 International Conference on Multimedia Technology*, Oct. 2010, pp. 1–3.

[141] P. Suresh, T. Thayaparan, and K. Venkataramaniah, "ISAR imaging of moving targets based on reassigned smoothed pseudo Wigner-Ville distribution," in *Proceedings of International Radar Symposium India, IRSI-2011*, 2011.

[142] I. Djurović and L. Stanković, "Time–frequency representation based on the reassigned S-method," *Signal processing*, vol. 77, no. 1, pp. 115–120, 1999.

[143] B. D. Rigling and R. L. Moses, "Taylor expansion of the differential range for monostatic SAR," *IEEE Transactions on Aerospace and Electronic Systems*, vol. 41, no. 1, pp. 60–64, Jan. 2005.

[144] E. Bishop, R. Linnehan, and A. Doerry, "Video-SAR using higher order taylor terms for differential range," in *2016 IEEE Radar Conference (RadarConf)*, Philadelphia, PA, USA, May 2016, pp. 1–4.

[145] P. O. Frolind and L. M. H. Ulander, "Evaluation of angular interpolation kernels in fast back-projection SAR processing," *IEE Proceedings on Radar, Sonar and Navigation*, vol. 153, no. 3, pp. 243–249, Jun. 2006.

Publications

Publication I

R. Vehmas, J. Jylhä, M. Väilä, J. Kylmälä, "A Computationally Feasible Optimization Approach to Inverse SAR Translational Motion Compensation", *2015 European Radar Conference (EuRAD)*, Paris, France, pp. 17 – 20, September 2015

Publication II

R. Vehmas, J. Jylhä, M. Väilä, A. Visa, "ISAR Imaging of Non-cooperative Objects with Non-uniform Rotational Motion", *2016 IEEE Radar Conference (RadarConf)*, Philadelphia, PA, USA, pp. 340–345, May 2016

Publication III

R. Vehmas, J. Jylhä, M. Väilä, A. Visa, "Analysis and Comparison of Multichannel SAR Imaging Algorithms", *2017 IEEE Radar Conference (RadarConf)*, Seattle, WA, USA, pp. 1–6, May 2017

Publication IV

R. Vehmas, J. Jylhä, M. Väilä, J. Vihonen, A. Visa, "Data-Driven Motion Compensation Techniques for Noncooperative ISAR Imaging", *IEEE Transactions on Aerospace and Electronic Systems*, vol. 54, no. 1, pp. 295 – 314, February 2018

Publication V

R. Vehmas, J. Jylhä, "Improving the Estimation Accuracy and Computational Efficiency of ISAR Range Alignment", *2017 European Radar Conference (EURAD)*, Nürnberg, Germany, pp. 13 – 16, October 2017

Publication VI

R. Vehmas, J. Jylhä, "A Contrast Optimization Algorithm for Back-Projection Image Reconstruction in Noncooperative ISAR Imaging", *EUSAR 2018; 12th European Conference on Synthetic Aperture Radar*, Aachen, Germany, pp. 464–469, June 2018

Tampereen teknillinen yliopisto
PL 527
33101 Tampere

Tampere University of Technology
P.O.B. 527
FI-33101 Tampere, Finland

ISBN 978-952-15-4227-5
ISSN 1459-2045